A LATTICE BOLTZMANN SCHEME WITH A THREE DIMENSIONAL CUBOID LATTICE

by

Haoda Min

A thesis submitted to the Faculty of the University of Delaware in partial fulfillment of the requirements for the degree of Master of Science in Mechanical Engineering

Spring 2016

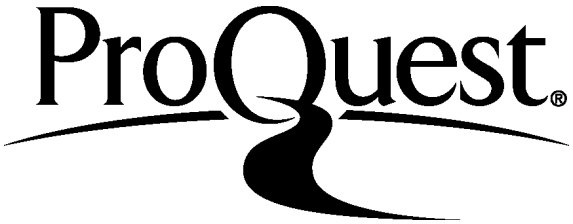

A LATTICE BOLTZMANN SCHEME WITH A THREE DIMENSIONAL CUBOID LATTICE

by

Haoda Min

Approved: _____

Lian-Ping Wang, Ph.D.
Professor in charge of thesis on behalf of the Advisory Commitee

Approved: _____

Suresh G. Advani, Ph.D.
Chair of the Department of Mechanical Engineering

Approved: _____

Babatunde A. Ogunnaike, Ph.D.
Dean of the College of Engineering

Approved: _____

Ann L. Ardis, Ph.D.
Senior Vice Provost for Graduate and Professional Education

ACKNOWLEDGMENTS

I would like to give my sincere gratitude to my advisor, Dr. Lian-Ping Wang for his inspiring encouragement and strong support in the past two years. It is an honor for me to have the great opportunity to work with him and learn from him. none of research work could be achieved without his rigorous training and earnest instruction.

I also want to express my gratitude to Dr. Leonard Schwartz, Dr. Joseph Feser for serving on the committee of my defense and providing many valuable comments and suggestions. I have also learned a lot of useful knowledge from the courses they offered.

Additionally, I am particularly grateful to my Lab mate Mr. Cheng Peng, who has given me countless of help and guidance on my research. I really appreciate his patience and assistance. Many thanks to my Lab mate, Mr. Sandipan Banerjee, Mr. Harish Opadrishta, Mr. Nicolas Geneva, Ms. Xin Wen and other friends for their kind assistance and encouragement. Special thanks to Ms. Jing Jin for giving me a great help on the revising of my thesis.

This work has been supported by the U.S. National Science Foundation (NSF) under grants CNS1513031, CBET-1235974, and AGS-1139743 and by Air Force Office of Scientific Research under grant FA9550-13-1-0213. I also acknowledges support from the Ministry of Education of P.R. China and Huazhong University of Science and Technology through Chang Jiang Scholar Visiting Professorship. I would like to acknowledge the travel support from U.S. National Science Foundation (NSF) to attend ICMMES-2015, held in CSRC (www.csrc.ac.cn), Beijing, July 20–24, 2015, under the Grant CBET-1549614. Thanks the National Center for Atmospheric Research and the University of Delaware for providing the computing resources through CISL-P35751014, CISL-UDEL0001 and NSF CRI 0958512.

TABLE OF CONTENTS

LIST OF TABLES . . . . . **vi**
LIST OF FIGURES . . . . . **viii**
ABSTRACT . . . . . **x**

Chapter

1 INTRODUCTION **1**

1.1 Introduction of the Lattice Boltzmann Method 1
1.2 Different Lattice Grids in the Lattice Boltzmann Method 3

1.2.1 Standard lattice model 3
1.2.2 Different non-standard lattice models 4

1.3 Mesoscopic Forcing Terms of LBM 6
1.4 Overview of the Thesis 8

2 INVERSE DESIGN OF D3Q19 MRT LBM ON A CUBOID LATTICE **10**

2.1 Basic Setup of the Proposed Lattice Boltzmann Model 10
2.2 The Chapman-Enskog Expansion and the Inverse Design Analysis . . 14
2.3 Summary of the Cuboid Lattice Model 22

3 NUMERICAL VALIDATIONS OF THE PROPOSED CUBOID LATTICE MODEL **27**

3.1 Transient Laminar Channel Flow 27
3.2 3D Decaying Taylor-Green Vortex Flow 31
3.3 Single Phase Turbulent Channel Flow 39
3.4 The Order of Accuracy of the Cuboid Model 43
3.5 Summary 48

4 CONCLUSION AND FUTURE WORKS **51**

4.1 Summary and Conclusions 51
4.2 Future Works 53

BIBLIOGRAPHY **55**

Appendix

A CALCULATION OF VELOCITY GRADIENTS **61**

LIST OF TABLES

1.1 Some previous efforts in developing LB models on non-standard lattices. 7

3.1 Parameter settings of the laminar channel flow with cuboid lattice grids. 29

3.2 Parameter settings of the 3D decaying Taylor-Green vortex flow. . . 33

3.3 Parameter settings of the turbulent channel flow. 41

3.4 The order of accuracy of the cuboid model evaluated with results from the transient laminar channel flow. The theoretical solutions are used as the benchmark. Results are calculated at $t\nu/H^2 = 1$. The streamwise velocity v is examined. 46

3.5 The L_1 error norm and the order of accuracy of the cuboid model evaluated with the 3D decaying Taylor-Green vortex flow. Results of the cuboid model with a resolution of $512 \times 640 \times 640$ are used as the benchmark to compute the error norms of the cuboid model at lower grid resolutions. Results are calculated at $2\pi U_0 t/L = 3$. 46

3.6 The L_2 error norm and the order of accuracy of the cuboid model evaluated with the 3D decaying Taylor-Green vortex flow. Results of the cuboid model with a resolution of $512 \times 640 \times 640$ are used as the benchmark to compute the error norms of the cuboid model at lower grid resolutions. Results are calculated at $2\pi U_0 t/L = 3$. 46

3.7 The L_1 error norm and the order of accuracy of the cuboid model evaluated with the 3D decaying Taylor-Green vortex flow. Results of the cuboid model with a resolution of $512 \times 640 \times 640$ are used as the benchmark to compute the error norms of the cuboid model at lower grid resolutions. Results are calculated at $2\pi U_0 t/L = 5$. 47

3.8 The L_2 error norm and the order of accuracy of the cuboid model evaluated with the 3D decaying Taylor-Green vortex flow. Results of the cuboid model with a resolution of $512 \times 640 \times 640$ are used as the benchmark to compute the error norms of the cuboid model at lower grid resolutions. Results are calculated at $2\pi U_0 t/L = 5$. 47

LIST OF FIGURES

1.1 The illustration of three different types of cubic lattice that are commonly used in the lattice Boltzmann method. 4

2.1 The illustration of D3Q19 cuboid lattice, the lattice sizes are different in three spatial directions. 10

3.1 The time evolution of the streamwise velocity v at $x/H = 0.4875$ (close to the channel centerline). All quantities are normalized as indicated. 29

3.2 The streamwise velocity profiles at six different times, $t\nu/H^2 = 0, 0.0248, 0.0537, 0.0958, 0.166$, and 1.24. All quantities are normalized as indicated. 30

3.3 The profiles of velocity gradient dv/dx at six different times, $t\nu/H^2 = 0, 0.0248, 0.0537, 0.0958, 0.166$, and 1.24. All quantities are normalized as indicated. 30

3.4 The time evolutions of (a) the average kinetic energy E_k, (b) the average dissipation rate ϵ. The results of two cuboid cases in Table 3.2 are compared to those of the two MRT-LBM cases with the cubic lattice and two different resolutions, the spectral method, and the short-time theory. 34

3.5 The time evolutions of (a) the velocity-derivative skewness, and (b) the velocity-derivative flatness. The results of two cuboid cases in Table 3.2 are compared to those of the two MRT-LBM cases with the cubic lattice and two different resolutions, the spectral method, and the short-time theory. 35

3.6 The velocity profiles on a line $x/L = 1/4$ and $y = z$ at the non-dimensional time $2\pi U_0 t/L = 5$. (a) Velocity in the x direction, (b) velocity in the y direction, and (c) velocity in the z direction. Results of the cuboid model are compared to results of the corresponding MRT-LBM with 64^3 cubic lattice. All quantities are normalized as indicated. 38

3.7 (a) The streamwise velocity averaged over the whole domain when the flow reaches the stationary stage. (b) Profiles of mean streamwise velocity as a function of x^+ when the flow reaches the stationary stage. All quantities are normalized as indicated. 42

3.8 (a) The Reynolds stress $-\langle u'v' \rangle / u_\tau^2$ profiles and (b) the r.m.s. velocity profiles. All quantities are normalized as indicated. 44

3.9 (a) The $L1$ error norm and (b) the $L2$ error norm of the streamwise velocity v in the laminar channel flow simulations. Results from four different aspect ratios are compared. 49

ABSTRACT

The lattice-Boltzmann method (LBM) is a mesoscopic computational scheme which solves the hydrodynamic (continuum) flow by using a set of discrete particle (or model molecular) velocities. The continuum flow evolution such as pressure and hydrodynamic velocity emerges as the average behaviors (*i.e.*, moments) of the mesoscopic model particles which undergo repeated collisions and propagations on a prescribed lattice. While LBM is now a viable alternative to convectional computational fluid dynamics (CFD) methods, it also has its limitations in terms of computational efficiency, which motivates this thesis work.

In the LBM simulation for fluid flow, the domain is usually discretized with a square lattice in 2D or a cubic lattice in 3D. Some previous studies were made to investigate the possibility of establishing a LBM model with non-standard lattice grid, namely, a rectangular lattice grid in 2D and a non-cubic (cuboid) lattice grid in 3D. The non-standard lattices are computationally more efficient when simulating a non-isotropic and inhomogeneous flows, *e.g.*, the turbulent channel flow.

In some previous non-standard lattice LBM developed by others, the Navier-Stokes equation is not correctly recovered because the resulting viscosity is anisotropic. The anisotropy is caused by the use of different lattice sizes in different directions; and it cannot be fixed without additional degrees of freedom. Recently at the University of Delaware, several new lattice Boltzmann schemes have been developed on a 2D rectangular grid using the multiple-relaxation-time (MRT) collision model, either by redesigning some moments to add a new free parameter, or by extending the equilibrium moments to include higher-order terms. These models can then satisfy all isotropy conditions as required by the Navier-Stokes equations.

In this thesis, based on the similar idea used in the successful design of LBM on a rectangular lattice, we developed a lattice Boltzmann model on a 3D cuboid lattice, namely, a lattice grid with different grid lengths in different spatial directions. Using the multi-scale Chapman-Enskog analysis, we designed the moment equations resulting from our MRT-LBM model, to be fully consistent with the Navier-Stokes equations. A second-order term is added to the equilibrium moments in order to not only satisfy all isotropy conditions but also to better accommodate different values of shear and bulk viscosities. The form of the second-order term and the coefficients of the extended equilibrium moments are determined through an inverse design process. An additional benefit of the model is that the shear viscosity can be adjusted, independent of the stress-moment relaxation parameter, thus improving the numerical stability of the model.

The resulting cuboid MRT-LBM model is then validated through several benchmark simulations, including the transient laminar channel flow, the fully developed single phase turbulent channel flow, and the 3D time-dependent, energy-cascading Taylor-Green vortex flow. In addition, the second-order accuracy of the proposed model is demonstrated in the simulation of 3D Taylor-Green vortex flow and transient laminar channel flow.

Chapter 1

INTRODUCTION

1.1 Introduction of the Lattice Boltzmann Method

Around 1990, a mesoscopic CFD (computational fluid dynamics) method known as the lattice Boltzmann equation (LBE) was created as a simulation tool for nearly incompressible fluid flows [1, 2]. LBE is a fully discrete form in both time and space of the kinetic Boltzmann equation, with a finite set of discrete molecular velocities [3, 4]. As a mesoscopic method based on the kinetic Boltzmann equation, the lattice Boltzmann method (LBM), or lattice Boltzmann model (LB model), has been developed rapidly in the last three decades. The basic idea of LBM is the realization that, in the continuum and incompressible limits, only a few conserved moments and a few non-conserved moments are required to reproduce the macroscopic hydrodynamic equations [4, 5, 6], namely, the continuity and the Navier-Stokes (N-S) equations. Therefore, instead of solving the N-S equations which have strong nonlinearity, the lattice Boltzmann method (LBM) solves the distribution functions that represent the number density of model discrete molecules with prescribed velocities [2, 4]. These discretized velocities are fully coupled with the lattice grid in the physical space and the time step size, which makes the numerical implementation of LBM highly efficient when compared to other kinetic schemes.

In LBE, the collision term is simplified by either the use of the single-relaxation-time Bhatnagar-Gross-Krook (BGK) [2, 4] model or the linearized multiple-relaxation-time (MRT) model [7, 8, 9]. LBE could be viewed as a compact discrete representation of the continuous Boltzmann equations, with a minimal set of discrete particles that can reproduce the required moments for continuum hydrodyamics [3, 4]. Each time

step in LBM consists of two sub-steps, namely, collision step and streaming step. In the collision step, the distribution functions are relaxed locally towards their equilibrium state. The only nonlinearity occurs in the evaluation of the equilibrium distribution in the collision operator, and this nonlinearity is fully local in the physical space. Then, in the streaming step, the updated distribution is advected according to the respective discrete particle velocity. This advection is exact, implying that LBM has very little numerical diffusion and dissipation. The macroscopic variables such as pressure, velocity and velocity gradients are then computed as the moments of the distribution functions.

In the BGK collision model, all hydrodynamic quantities are relaxed to their equilibrium state at the same rate [2, 4]. Thus, their relaxation parameters are identical, which leads to some apparent drawback of this collision model. For example, the Prandtl number $Pr = \nu/\alpha$ in the lattice BGK model is restricted to one [4], where ν is the shear viscosity and α represents the thermal diffusivity. The viscosity in the standard lattice BGK model is related to this relaxation parameter. To achieve a high flow Reynolds number (Re), a small viscosity is usually required. At the same time, the relaxation parameter is known to be related to the numerical stability. Therefore, LBM simulation of high Re flows often encounters numerical instability, and there is no flexibility to separate the physical goal of simulating high-Re flows and computational goal of creating a robust and stable numerical method [10, 11]

This problem motivated the use of the multiple-relaxation time (MRT) collision model, where different moments are allowed to relax at different rates through a linear matrix multiplication [7, 8, 9]. By doing so, one could have more flexibility of assigning the values of different relaxation parameters, as the relaxation parameters for at least some moments are decoupled from the fluid viscosity so they can be optimized to enhance the stability of LBM [10, 11].

Although the method solves more variables than the conventional CFD methods based on integrating directly the Navier-Stokes (N-S) equations. Several features

of the LBM are highly valued: simplicity of the algorithm and implementation, excellent capability of handling complex geometrics [12, 13, 14, 15], highly parallelizable since the collision process is completely local and the propagation only involves data communication with neighboring nodes [5, 6, 16]. With these advantages, the LBM has been developed rapidly in the last three decades and applied extensively for fluid dynamics simulations in many different areas such as hydrodynamic systems, magneto-hydrodynamic systems, multiphase and multicomponent fluid flows, chemical-reactive flows, and flow through porous media [17, 18, 19, 20, 21]. LBM is a highly competitive method for multiphase flows or flows with complex boundaries [12, 13, 15, 22, 23, 24].

1.2 Different Lattice Grids in the Lattice Boltzmann Method

1.2.1 Standard lattice model

The standard lattice grids are adopted in most previous flow simulations using LBM, namely, a square lattice in 2D and a cubic lattice in 3D. For 2D problems, the typical choice of lattice is the D2Q9 lattice [4], where "D" represents the dimension of the problem, and "Q" represents the number of discretized velocity implemented on the lattice grid. In the D2Q9 lattice, 8 discrete non-zero velocities are directed to the neighboring nodes, along with a rest particle. For 3D problems, three different types of standard lattices are usually adopted, namely, D3Q15, D3Q19 and D3Q27 [8, 25], as illustrated in Fig. 1.1. All these lattice grids share a common feature, namely, the lattice sizes in different spatial directions are identical, namely, geometrically isotropic. This feature makes the standard lattice grids to be easily implemented. However, the computational efficiency of standard lattice is limited when LBM is applied to non-isotropic and inhomogeneous flows, in particular, wall-bounded turbulent flows. For example, in the simulation of a fully developed turbulent channel flow, it is suggested that the domain size in the streamwise direction be made much longer than the transverse direction to reduce the effect of streamwise correlation length [26]. As a result, a very large number of lattice cells must be used in the streamwise direction to fill the domain, as the lattice size is governed by the the smallest scale in the wall-normal

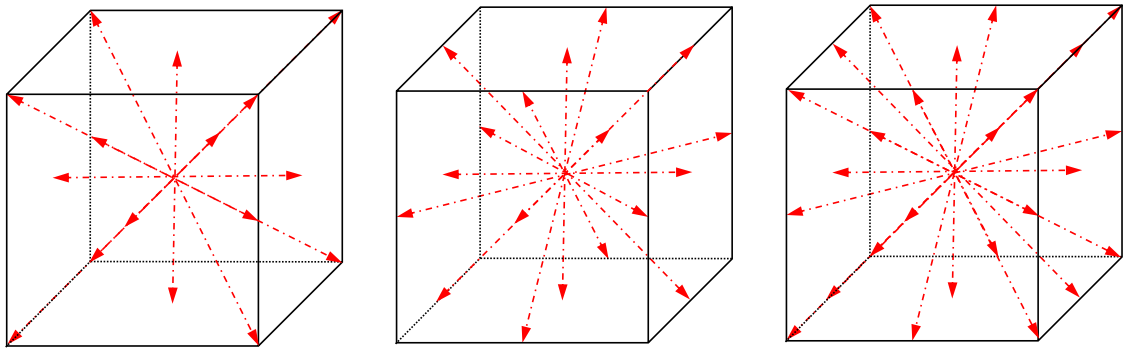

Figure 1.1: The illustration of three different types of cubic lattice that are commonly used in the lattice Boltzmann method.

direction which is much smaller than the smallest scale in the streamwise direction. Therefore, the standard, geometrically-isotropic lattice grid is clearly computationally inefficient.

1.2.2 Different non-standard lattice models

In order to remove the drawback of standard LBM, several efforts have been made to incorporate a more general (*i.e.*, nonuniform or anisotropic) grid into LBM. These efforts could be divided into the following four groups.

The first group utilizes spatial and temporal interpolation schemes to couple the inherent lattice grid with a general computation grid on which the hydrodynamic variables are solved [27, 28]. Although such implementations allow more flexibility of the computational grid structure [29], the accuracy of such two-grid implementations is still determined by the inherent standard lattice. Furthermore, the interpolations introduce additional numerical errors and artificial viscosity to the flow system being solved. The second group chooses to replace the exact streaming operation in LBM with a finite-difference scheme or other discretization schemes [30, 31], in order to remove the usual coupling between lattice space and lattice time. This type of implementations not only causes additional numerical diffusion and dissipation, but could be more

complicated and computationally more expensive, *e.g.*, additional data communication may be required.

Different from the above, the third group incorporates directly a non-standard lattice grid such as a rectangular grid in 2D, by modifying the kinetic particle velocities to fit the lattice grid. The use of a rectangular grid immediately introduces anisotropy which must be corrected by a proper re-design of the collision operator. This approach preserves all the appealing features of the standard LBM, *i.e.,* the inherent simplicity, numerical accuracy, and computational efficiency. Bouzidi *et al.* [32] was the first to propose a D2Q9 LBM using anisotropic particle velocities to fit a rectangular lattice grid. Their LBM scheme made use of the MRT collision operator. They modified the definitions of moments and their model is almost consistent with the Navier-Stokes equations, except that the shear and bulk viscosities are not strictly isotropic when the grid aspect ratio differs from one, as shown by Zong [33]. Similar attempts were made by Zhou who proposed two models with both BGK [34] and MRT [35] collision operators. However, neither of his models is consistent with the N-S equations [33, 36]. Hegele *et al.* [37] claimed that, for the standard D2Q9 lattice and D3Q19 lattice, the degrees of freedom are not enough to remove the anisotropy resulting from the use of the non-isotropic lattice grid, when the BGK collision operator is used. Thus they suggested to extend these lattices to D2Q11 and D3Q23, respectively, to recover the N-S equations. Their D2Q11 model was indeed validated on a rectangular grid using the 2D Taylor-Green vortex flow. Lastly, a D3Q19 model with a cuboid lattice is proposed by Jiang and Zhang for pore-scale simulation of fluid flow in porous media [38]. In their model, the anisotropy of viscosity is fixed by adopting different relaxation parameters in different spatial directions. In their model, the lattice length of the cuboid could be different in three directions. However, even for a laminar pipe flow, the aspect ratio can only be in the narrow range from 0.8 to 1.25 due to stability consideration. In addition, their result cannot match the analytical solution exactly. An apparent deviation could be observed on the velocity profile especially near the pipe center.

In the last group of works, the anisotropic problem of viscosity in the non-standard lattice LB model has recently been fixed by a re-design of the moments that introduces extra degrees of freedom, or by modifying the equilibrium moments, or both. Zong *et al.* [33] extended Bouzidi *et al.* 's model by introducing a parameter θ to reconfigure the two-dimensional energy-normal stress moment sub-space. For a given grid aspect ratio, a unique θ value is determined to restore the full isotropy condition required by the N-S equations. An alternative and more general LBM MRT model on a rectangular grid has been developed by Peng *et al.* [39] who instead incorporated stress components into the equilibrium moments to remove the anisotropy in the stress tensor resulting from the use of a rectangular lattice. Such an approach was previously used by Inamuro [40] to improve the stability of LBGK model, and later by Yoshino *et al.* [41] and Wang *et al.* [42] to treat non-Newtonian fluid flows. The generality of the extended-equilibrium approach has also been explored using the simpler BGK collision model by Peng *et al.* [43] who in fact showed that even an LBGK model can be successfully extended to work on a rectangular grid. Such was not thought to be possible previously. The key in all these three successful models on a rectangular grid [33, 39, 43] is to combine new constraints and new adjustable parameters to satisfy all isotropy conditions required by the N-S equations.

1.3 Mesoscopic Forcing Terms of LBM

As a mesoscopic method with larger degrees of freedom relative to the continuum description of fluid flow, the LBM has a greater design flexibility than its conventional CFD counterparts, and such flexibility is yet to be fully explored. This flexibility originates partially from the fact that the mesoscopic distribution functions contain more information than the moments governed by the continuity and the N-S equations. Many fluid dynamics problems could involve external forces that are non-uniform and time-dependent, especially in turbulent flows or multiphase flows [22, 23, 24]. For instance, in the simulation of forced homogeneous turbulence, the turbulent kinetic

Table 1.1: Some previous efforts in developing LB models on non-standard lattices.

Chronological	Collision scheme & Lattice type	Comments
Bouzidi *et al.* (2001)	MRT & D2Q9 rectangular	Partially fixed the anisotropy of viscosity by set a restriction for three relaxation parameters; not fully consistent with the N-S equations
Hegele *et al.* (2013)	MRT & D2Q11 rectangular	Increase the number of discretized particle velocities; consistent with the N-S equations
Jiang *et al.* (2014)	BGK & D3Q19 cuboid	Adop different relaxation parameters in different spatial directions; consistent with the N-S equations; the aspect ratio is limited in a narrow range from 0.8 to 1.25 even for laminar flow
Zong *et al.* (2015)	MRT & D2Q9 rectangular	Re-design two equilibrium moments to introduce one extra degree of freedom; consistent with the N-S equations
Peng *et al.* (2016)	MRT & D2Q9 rectangular	Extend the equilibrium moments to introduce extra degrees of freedom; consistent with the N-S equations
Peng *et al.* (2016)	BGK & D2Q9 rectangular	Extend the equilibrium distributions to introduce extra degrees of freedom; consistent with the N-S equations;

energy is added into the computational domain with non-uniform time-dependent forcing [22, 23]. These forces are often formulated at the continuum level, and as such they need to be converted into a mesoscopic form. Whether this conversion is designed appropriately affects the accuracy and consistency of the resulting hydrodynamics. For example, it has been shown that the mesoscopic forcing could affect velocity gradient and strain-rate components calculated from the non-equilibrium moments [44].

Previously, the mesoscopic representation of a forcing term has been widely studied with the BGK collision operators in [45, 46, 47, 48, 49, 50, 51]. Advantages and disadvantages of different forcing implementations based on the BGK model have also been compared [51, 52, 53]. Guo *et al.* [51] derived a mesoscopic forcing, based on a rigorous Chapman-Enskog expansion, that is fully consistent with the N-S equation and maintains the second-order accuracy of the LBM scheme. Guo's forcing scheme has been extended to the LB models with MRT collision operator and standard lattice grid [44, 54], and rectangular lattice grid [55].

In this thesis, a general form of the mesoscopic forcing terms of the proposed MRT LB model with cuboid lattice will be derived from a rigorous inverse design process. The mesoscopic forcing terms will be added to the lattice Boltzmann equation to represent the macroscopic external forces on the mesoscopic level so that other mesoscopic quantities will be affected by the external forces.

1.4 Overview of the Thesis

The objective of this thesis is to develop a D3Q19 MRT LBM model on a general cuboid grid with grid spacing ratios given as $\delta_x : \delta_y : \delta_z = 1 : a : b$, using a D3Q19 lattice. The basic idea of the approach follows closely the 2D extended-moment method described in [39].

The remainder of the thesis is organized as follows: The derivation of the proposed cuboid lattice model by the Chapman-Enskog analysis and an inverse design process is presented in Chapter 2. The most general form of the cuboid lattice model will be derived based on the requirements of the hydrodynamic equations. Additionally,

a general non-uniform mesoscopic forcing term will also be added, at the mesoscopic level, to represent the macroscopic force so that the model could handle a flow with any kind of external force. Moreover, the correct hydrodynamic equations and isotropic viscosity will be achieved since the idea of inverse design is applied.

In Chapter 3, careful validations of the model are provided using three different flows, namely, the transient laminar channel flow, the 3D energy-cascading Taylor-Green vortex flow [56], and the fully-developed turbulent channel flow. In the transient laminar channel flow, the results of cuboid lattice model will be compared to the theoretical results. In the turbulent channel flow and the 3D Taylor-Green vortex flow, the cuboid model will be compared to the spectral method and theoretical results when available. Finally, the order of accuracy of this model will be examined by using the laminar channel flow and the 3D decaying Taylor-Green vortex flow. A second-order accuracy will be shown for both velocity and stress components calculated by the proposed cuboid lattice model.

Finally, in Chapter 4 we summarize key conclusions for the proposed MRT LBM on a cuboid lattice . Possible future directions will also be presented.

Chapter 2

INVERSE DESIGN OF D3Q19 MRT LBM ON A CUBOID LATTICE

In this section, we shall design and derive a D3Q19 MRT LBM model on *a cuboid grid* that is fully consistent with the N-S equation with a time-dependent and spatially non-uniform forcing $\mathbf{F} \equiv (F_x, F_y, F_z)$.

2.1 Basic Setup of the Proposed Lattice Boltzmann Model

For a cuboid lattice, the lattice spacings can be different in the three spatial directions. Without loss of the generality, we set the lattice spacing in the x direction to $\delta_x = 1$, and assume the grid spacing in y and z directions to be $a\delta_x$ and $b\delta_x$, respectively. Thus, a and b are defined as $a = \delta_y/\delta_x$, $b = \delta_z/\delta_x$, where δ_x $[m]$, δ_y $[m]$ and δ_z $[m]$ are the lattice sizes in the three directions, respectively. The physical units for key quantities are indicated to help validate the unit consistency of our model. A sketch of the cuboid lattice is shown in Fig. 2.1. Therefore, the corresponding discrete velocities on the D3Q19 cuboid lattice are

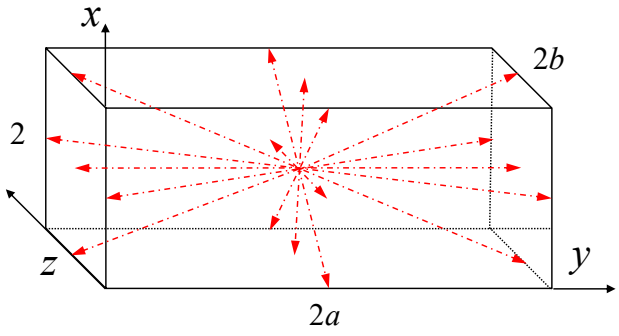

Figure 2.1: The illustration of D3Q19 cuboid lattice, the lattice sizes are different in three spatial directions.

$$\mathbf{e}_i = \begin{cases} (0,0,0)\,c, & i = 0 \\ (\pm 1,0,0)\,c, (0,\pm a,0)\,c, (0,0,\pm b)\,c, & i = 1-6 \\ (\pm 1,\pm a,0)\,c, (\pm 1,0,\pm b)\,c, (0,\pm a,\pm b)\,c, & i = 7-18 \end{cases} \tag{2.1}$$

where $c = \delta_x/\delta_t$ $[m \cdot s^{-1}]$ is the non-zero lattice velocity component in the x direction, δ_t $[s]$ is the time step size.

The distribution functions in the cuboid-lattice LBM scheme evolve according to the same lattice Boltzmann equation (LBE) with the multiple relaxation time (MRT) collision model, as

$$f_i(\mathbf{x} + \mathbf{e}_i\delta_t, t + \delta_t) - f_i(\mathbf{x}, t) = -\mathbf{M}^{-1}\mathbf{S}\left[\mathbf{m}(\mathbf{x}, t) - \mathbf{m}^{eq}(\mathbf{x}, t)\right] + \Phi_i, \tag{2.2}$$

where f_i is the distribution function associated with the kinetic velocity $\mathbf{e}_i$, $\mathbf{x}$ and t are the spatial and time coordinates, respectively. The first term on the right hand side of Eq. (2.2) describes the MRT collision operator and the second term Φ_i $[kg \cdot m^{-3}]$ is used to represent the mesoscopic forcing term which accounts for the effect of macroscopic forcing $\mathbf{F} \equiv (F_x, F_y, F_z)$ $[kg \cdot m^{-2} \cdot s^{-2}]$. The components of Φ_i will be designed by an inverse design analysis.

The transformation matrix $\mathbf{M}$ converts the distribution functions f_i to the moments $\mathbf{m}$ by $\mathbf{m} = \mathbf{M}\mathbf{f}$, and vise versa $\mathbf{f} = \mathbf{M}^{-1}\mathbf{m}$, where $\mathbf{f}$ denotes a vector containing f_i. The equilibrium moments are denoted by $\mathbf{m}^{(eq)}$. For simplicity, the moments are defined in a manner identical to the standard D3Q19 MRT model [8]. Each discrete velocity $\mathbf{e}_i$ may have different velocity magnitudes in the three spatial directions. In order to keep the same simple transformation matrix as in the cubic-lattice D3Q19 model, we first normalize the velocity components differently in different directions, namely, the transformation matrix and the moments are defined based on the normalized components e_{ix}/c, $e_{iy}/(a \cdot c)$, and $e_{iz}/(b \cdot c)$. The similar normalizations were used by Zhou [35] in his attempt to develop a D2Q9 rectangular-grid model. Therefore, the normalized components are identical to those in the standard cubic-lattice D3Q19

model. The transformation matrix is then written as [8]

$$
\mathbf{M} = \begin{bmatrix}
1 & 1 & 1 & 1 & 1 & 1 & 1 & 1 & 1 & 1 & 1 & 1 & 1 & 1 & 1 & 1 \\
-30 & -11 & -11 & -11 & -11 & 8 & 8 & 8 & 8 & 8 & 8 & 8 & 8 & 8 & 8 & 8 \\
12 & -4 & -4 & -4 & -4 & 1 & 1 & 1 & 1 & 1 & 1 & 1 & 1 & 1 & 1 & 1 \\
0 & 1 & -1 & 0 & 0 & 0 & 1 & -1 & 1 & -1 & 1 & -1 & 1 & -1 & 0 & 0 \\
0 & -4 & 4 & 0 & 0 & 0 & 1 & -1 & 1 & -1 & 1 & -1 & 1 & -1 & 0 & 0 \\
0 & 0 & 0 & 1 & -1 & 0 & 1 & -1 & -1 & 1 & 0 & 0 & 1 & -1 & 1 & -1 \\
0 & 0 & 0 & -4 & 4 & 0 & 0 & 1 & -1 & -1 & 1 & 0 & 0 & 1 & -1 & 1 \\
0 & 0 & 0 & 0 & 0 & 1 & -1 & 0 & 0 & 0 & 0 & 1 & -1 & -1 & 1 & -1 \\
0 & 2 & 2 & -1 & -1 & -1 & -1 & 4 & 4 & -1 & -1 & 1 & 1 & 1 & -1 & 1 \\
0 & -4 & -4 & 2 & 2 & 2 & 2 & 2 & 2 & -1 & -1 & 1 & 1 & 1 & -1 & 1 \\
0 & 0 & 0 & 1 & -1 & 0 & 0 & 0 & 0 & 1 & -1 & -1 & 1 & -1 & 1 & -1 \\
0 & 0 & 0 & -2 & 2 & 0 & 0 & 0 & 0 & 1 & -1 & -1 & 1 & -1 & 1 & -1 \\
0 & 0 & 0 & 0 & 0 & 0 & 0 & 0 & 0 & 1 & -1 & -1 & 1 & -1 & 1 & -1 \\
0 & 0 & 0 & 0 & 0 & 0 & 0 & 0 & 0 & 1 & -1 & -1 & 1 & -1 & 1 & -1 \\
0 & 0 & 0 & 0 & 0 & 0 & 0 & 0 & 0 & 0 & -1 & -1 & 1 & -1 & 1 & -1 \\
0 & 0 & 0 & 0 & 0 & 0 & 0 & 0 & 0 & 0 & 0 & 0 & 1 & -1 & 1 & -1
\end{bmatrix}
\tag{2.3}
$$

where the row vectors of $\mathbf{M}$ are orthogonal with each other, so are those column vectors in the inverse matrix $\mathbf{M^{-1}}$ [7]. The individual moments thus derived by $\mathbf{m} = \mathbf{Mf}$ are

denoted as

$$\mathbf{m} = |\tilde{\rho}, e, \varepsilon, j_x, q_x, j_y, q_y, j_z, q_z, 3p_{xx}, \pi_{xx}, p_{ww}, \pi_{ww}, p_{xy}, p_{yz}, p_{xz}, m_x, m_y, m_z\rangle\,, \tag{2.4}$$

where $\tilde{\rho}$ $[kg \cdot m^{-3}]$ is the zeroth-order moment representing local density fluctuation, namely, $\tilde{\rho} = \rho - \rho_0 \equiv \delta\rho$ (ρ and ρ_0 are the density and the average density, respectively); e $[kg{\cdot}m^{-1}{\cdot}s^{-2}]$ is a second-order moment related to the energy; ε $[kg{\cdot}m{\cdot}s^{-4}]$ is a fourth-order moment associated with the square of energy; j_x, j_y, j_z $[kg{\cdot}m^{-2}{\cdot}s^{-1}]$ are the three first-order moments connected to the momentum in x, y and z direction, respectively; q_x, q_y, q_z $[kg \cdot s^{-3}]$ are three third-order moments related to the energy flux in x, y and z direction, respectively; p_{xx}, p_{ww} $[kg \cdot m^{-1} \cdot s^{-2}]$ are two second-order moments corresponding to the normal stress components; p_{xy}, p_{yz}, p_{xz} $[kg \cdot m^{-1} \cdot s^{-2}]$ are the other three second-order moments related to the shear-stress components; m_x, m_y, m_z are all third-order moments that can be regarded as the normal stress flux; π_{xx} and π_{ww} $[kg{\cdot}m{\cdot}s^{-4}]$ are the fourth-order moments derived from products between energy mode and normal stress mode. Note that the density has been partitioned as in [4] to better reproduce the incompressible N-S equations. In summary, in the D3Q19 model, we have one zeroth-order moment ($\tilde{\rho}$), three first-order moments (j_x, j_y, j_z), six second-order moments ($e, p_{xx}, p_{ww}, p_{xy}, p_{yz}, p_{xz}$), six third-order moments ($q_x, q_y, q_z, m_x, m_y, m_z$), and three fourth-order moments ($\varepsilon, \pi_{xx}, \pi_{ww}$). These are all the independent moments that can be formed.

As we shall show later, all the moments at the third order or below can be uniquely determined in our inverse design process, while the three fourth-order moments are irrelevant to the N-S equations.

The diagonal relaxation matrix $\mathbf{S}$ specifies all dimensionless relaxation parameters

$$\mathbf{S} = diag(s_{\tilde{\rho}}, s_e, s_\varepsilon, s_j, s_q, s_j, s_q, s_j, s_q, s_n, s_\pi, s_n, s_\pi, s_c, s_c, s_c, s_m, s_m, s_m), \tag{2.5}$$

where $s_{\tilde{\rho}}$ is the relaxation parameter for the zeroth-order moment ($\tilde{\rho}$); s_j is the relaxation parameter for the first-order moments (j_x, j_y, j_z); three relaxation parameters are

introduced for the six second-order moments: s_e for energy (e), s_n for the normal-stress moments (p_{xx}, p_{ww}), and s_c for the shear-stress moments (p_{xy}, p_{yz}, p_{xz}); two relaxation parameters are used for the six third-order moments: s_q for energy flux moments (q_x, q_y, q_z) and s_m for normal-stress flux moments (m_x, m_y, m_z); finally, two relaxation parameters are specified for the three fourth-order moments: s_ε for energy square moment (ε) and s_π for the energy-stress coupling terms (π_{xx}, π_{ww}). As mentioned in the Introduction, we need to overcome the anisotropic transport coefficients that are originated by the anisotropic lattice velocities, in order to reproduce the N-S equations. In this work, we follow the same idea as in [39], namely, the equilibrium moments are extended to include a higher-oder term as $\mathbf{m}^{(eq)} = \mathbf{m}^{(eq,0)} + \epsilon \mathbf{m}^{(eq,1)}$, where ϵ is a small parameter that is proportional to the Knudsen number. The higher-order term $\epsilon \mathbf{m}^{(eq,1)}$ will be expressed in terms of stress components.

2.2 The Chapman-Enskog Expansion and the Inverse Design Analysis

Next, a detailed Chapman-Enskog analysis will be performed to design the components of the equilibrium moment $\mathbf{m}^{(eq)}$ and the mesoscopic forcing term $\mathbf{\Phi}$. Following the standard procedure, the Taylor expansion with respect to time and location is applied to $f_i(\mathbf{x} + \mathbf{e}_i\delta_t, t + \delta_t)$ in Eq. (2.2). After multiplying by $\mathbf{M}/\delta_t$, we obtain

$$\left(\mathbf{I}\partial_t + \hat{\mathbf{C}}_\alpha \nabla_\alpha\right)\mathbf{m} + \frac{\delta_t}{2}\left(\mathbf{I}\partial t + \hat{\mathbf{C}}_\alpha \nabla_\alpha\right)^2 \mathbf{m} = -\frac{\mathbf{S}}{\delta_t}\left(\mathbf{m} - \mathbf{m}^{(eq)}\right) + \mathbf{\Psi}, \tag{2.6}$$

where $\mathbf{I}$ is an identity matrix, $\mathbf{\Psi} \equiv \mathbf{M}\mathbf{\Phi}/\delta_t$ denotes the moments associated with the forcing term, ∂_t stands for the time derivative, ∇_α with $\alpha = x$, y, or z denotes the spatial derivatives, and $\hat{\mathbf{C}}_\alpha \equiv \mathbf{M} diag(e_{i\alpha})\mathbf{M^{-1}}$. The following multiscale expansion is

now applied to $\mathbf{m}$, $\mathbf{m}^{(eq)}$, ∂_t, ∇_α, and $\mathbf{\Psi}$ [50, 51] :

$$\mathbf{m} = \mathbf{m}^{(0)} + \epsilon\ \mathbf{m}^{(1)} + \epsilon^2 \mathbf{m}^{(2)} + ..., \tag{2.7a}$$

$$\mathbf{m}^{(eq)} = \mathbf{m}^{(eq,0)} + \epsilon\ \mathbf{m}^{(eq,1)}, \tag{2.7b}$$

$$\partial_t = \epsilon\ \partial_{t1} + \epsilon^2 \partial_{t2}, \tag{2.7c}$$

$$\nabla_\alpha = \epsilon\ \nabla_{1\alpha}, \tag{2.7d}$$

$$\mathbf{\Psi} = \epsilon\ \mathbf{\Psi}^{(1)}. \tag{2.7e}$$

Once again, the most significant difference here is that the multiscale expansion is also applied to the equilibrium moments $\mathbf{m}^{(eq)}$. Substituting Eq. (2.7) into Eq. (2.6) and rearranging the equation according to $\mathcal{O}(\epsilon)$, we obtain the following three equations

$$\mathcal{O}(1):\ \mathbf{m}^{(0)} = \mathbf{m}^{(eq,0)}, \tag{2.8a}$$

$$\mathcal{O}(\epsilon):\ \left(\mathbf{I}\partial_{t1} + \hat{\mathbf{C}}_\alpha \partial_{1\alpha}\right)\mathbf{m}^{(0)} = -\frac{\mathbf{S}}{\delta_t}\left(\mathbf{m}^{(1)} - \mathbf{m}^{(eq,1)}\right) + \mathbf{\Psi}^{(1)}, \tag{2.8b}$$

$$\begin{aligned}\mathcal{O}(\epsilon^2):\ \partial_{t2}\mathbf{m}^{(0)} + \left(\mathbf{I}\partial_{t1} + \hat{\mathbf{C}}_\alpha \partial_{1\alpha}\right)\left[\left(\mathbf{I} - \frac{\mathbf{S}}{2}\right)\mathbf{m}^{(1)} + \frac{\mathbf{S}}{2}\mathbf{m}^{(eq,1)} + \frac{\delta_t}{2}\mathbf{\Psi}^{(1)}\right] \\ = -\frac{\mathbf{S}}{\delta_t}\mathbf{m}^{(2)}.\end{aligned} \tag{2.8c}$$

Each equation in Eq. (2.8) is a vector equation containing 19 scalar-moment equations. Based on the ordering of moments we defined in Eq. (2.4), the first row of Eq. (2.8b) and (2.8c) should correspond to the continuity equation. The 4^{th}, 6^{th} and 8^{th} row of Eq. (2.8b) and (2.8c) should correspond to the hydrodynamic momentum equations in x, y and z directions, respectively.

Since density is a conserved moment, we set $\tilde{\rho}^{(0)} = \tilde{\rho}^{(eq,0)} = \delta\rho$ and $s_{\tilde{\rho}} = 0$. Therefore, $\tilde{\rho}^{(k)} = 0$ for $k \geq 1$. The first row of Eq. (2.8b) thus becomes

$$\partial_{t1}\delta\rho + \partial_{1x} j_x^{(0)} + a\partial_{1y} j_y^{(0)} + b\partial_{1x} j_z^{(0)} = \frac{s_{\tilde{\rho}}}{\delta_t}\tilde{\rho}^{(eq,1)} + \Psi_1^{(1)}, \tag{2.9}$$

which should reproduce the continuity equation at $\mathcal{O}(\epsilon)$ to the leading order

$$\partial_{t1}\delta\rho + \partial_{1x}(\rho_0 u) + \partial_{1y}(\rho_0 v) + \partial_{1z}(\rho_0 w) = 0. \tag{2.10}$$

Therefore, by comparing Eq. (2.9) with Eq. (2.10), we obtain $j_x^{(0)} = \rho_0 u$, $j_y^{(0)} = \rho_0 v/a$, $j_z^{(0)} = \rho_0 w/b$. Since the density should not be affected by the forcing, we must have $\Psi_1^{(1)} = 0$, and thus $\tilde{\rho}^{(eq,1)} = 0$.

Likewise, the $4^{th}, 6^{th}$ and 8^{th} row of Eq. (2.8b)

$$\begin{aligned} &\partial_{t1}\left(\rho_0 u\right) + \partial_{1x}\left(\frac{10}{19}c^2\delta\rho + \frac{1}{57}e^{(0)} + \frac{1}{3}p_{xx}^{(0)}\right) + a\partial_{1y}\left(p_{xy}^{(0)}\right) \\ &\qquad + b\partial_{1z}\left(p_{xz}^{(0)}\right) = -\frac{s_j}{\delta_t}\left(j_x^{(1)} - j_x^{(eq,1)}\right) + \Psi_4^{(1)}, \end{aligned} \tag{2.11a}$$

$$\begin{aligned} &\partial_{t1}\left(\frac{\rho_0 v}{a}\right) + a\partial_{1y}\left(\frac{10}{19}c^2\delta\rho + \frac{1}{57}e^{(0)} - \frac{1}{6}p_{xx}^{(0)} + \frac{1}{2}p_{ww}^{(0)}\right) + \partial_{1x}\left(p_{xy}^{(0)}\right) \\ &\qquad + b\partial_{1z}\left(p_{yz}^{(0)}\right) = -\frac{s_j}{\delta_t}\left(j_y^{(1)} - j_y^{(eq,1)}\right) + \Psi_6^{(1)}, \end{aligned} \tag{2.11b}$$

$$\begin{aligned} &\partial_{t1}\left(\frac{\rho_0 w}{b}\right) + b\partial_{1z}\left(\frac{10}{19}c^2\delta\rho + \frac{1}{57}e^{(0)} - \frac{1}{6}p_{xx}^{(0)} - \frac{1}{2}p_{ww}^{(0)}\right) + \partial_{1x}\left(p_{xz}^{(0)}\right) \\ &\qquad + a\partial_{1y}\left(p_{yz}^{(0)}\right) = -\frac{s_j}{\delta_t}\left(j_z^{(1)} - j_z^{(eq,1)}\right) + \Psi_8^{(1)}, \end{aligned} \tag{2.11c}$$

must match the following Euler momentum equations

$$\partial_{t1}(\rho_0 u) + \partial_{1x}\left(p + \rho_0 u^2\right) + \partial_{1y}\left(\rho_0 uv\right) + \partial_{1z}\left(\rho_0 uw\right) = F_x^{(1)}, \tag{2.12a}$$

$$\partial_{t1}(\rho_0 v) + \partial_{1y}\left(p + \rho_0 v^2\right) + \partial_{1x}\left(\rho_0 uv\right) + \partial_{1z}\left(\rho_0 vw\right) = F_y^{(1)}, \tag{2.12b}$$

$$\partial_{t1}(\rho_0 w) + \partial_{1z}\left(p + \rho_0 w^2\right) + \partial_{1x}\left(\rho_0 uw\right) + \partial_{1y}\left(\rho_0 vw\right) = F_z^{(1)}. \tag{2.12c}$$

In Eq. (2.12) the pressure is expressed as $p = \delta\rho c_s^2$ for isothermal flows, where c_s $[m \cdot s^{-1}]$ is the speed of sound. Consistency of the left hand sides of Eq. (2.11) and Eq. (2.12) leads to the following results

$$e^{(0)} = 19\delta\rho(c_s^2 + \frac{c_s^2}{a^2} + \frac{c_s^2}{b^2} - \frac{30}{19}c^2) + 19\rho_0(u^2 + \frac{v^2}{a^2} + \frac{w^2}{b^2}), \tag{2.13a}$$

$$p_{xx}^{(0)} = \delta\rho(2c_s^2 - \frac{c_s^2}{a^2} - \frac{c_s^2}{b^2}) + \rho_0(2u^2 - \frac{v^2}{a^2} - \frac{w^2}{b^2}), \tag{2.13b}$$

$$p_{ww}^{(0)} = \delta\rho c_s^2\frac{b^2 - a^2}{a^2 b^2} + \rho_0(\frac{v^2}{a^2} - \frac{w^2}{b^2}), \tag{2.13c}$$

$$p_{xy}^{(0)} = \frac{\rho_0 uv}{a}, \quad p_{xz}^{(0)} = \frac{\rho_0 uw}{b}, \quad p_{yz}^{(0)} = \frac{\rho_0 vw}{ab}. \tag{2.13d}$$

And a comparison of the right hand sides of Eq. (2.11) and Eq. (2.12) yields

$$-\frac{s_j}{\delta_t}j_x^{(1)}+\frac{s_j}{\delta_t}j_x^{(eq,1)}+\Psi_4^{(1)}=F_x^{(1)}, \tag{2.14a}$$

$$-\frac{s_j}{\delta_t}j_y^{(1)}+\frac{s_j}{\delta_t}j_y^{(eq,1)}+\Psi_6^{(1)}=\frac{F_y^{(1)}}{a}, \tag{2.14b}$$

$$-\frac{s_j}{\delta_t}j_z^{(1)}+\frac{s_j}{\delta_t}j_z^{(eq,1)}+\Psi_8^{(1)}=\frac{F_z^{(1)}}{b}. \tag{2.14c}$$

Next, we proceed to compare the moment equations on the order of $\mathcal{O}(\epsilon^2)$ with the N-S equations on the order of $\mathcal{O}(\epsilon^2)$. For simplicity, we define

$$\mathbf{A}\equiv\left(\mathbf{I}-\frac{\mathbf{S}}{2}\right)\mathbf{m}^{(1)}+\frac{\mathbf{S}}{2}\mathbf{m}^{(eq,1)}+\frac{\delta_t}{2}\mathbf{\Psi}^{(1)}, \tag{2.15}$$

which simplifies Eq. (2.8c) to

$$\mathcal{O}\left(\epsilon^2\right):\partial_{t2}\mathbf{m}^{(0)}+(\mathbf{I}\partial_{t1}+\hat{\mathbf{C}}_\alpha\partial_{1\alpha})\mathbf{A}=-\frac{\mathbf{S}}{\delta_t}\mathbf{m}^{(2)}. \tag{2.16}$$

Since we have shown that $\rho_1^{(1)}=\rho_1^{(eq,1)}=0$ and $\Psi_1^{(1)}=0$, it follows that the first element of $\mathbf{A}$, namely, A_1, should also be zero. Then the 1^{st} row of Eq. (2.16) reads

$$\partial_{t2}\delta\rho+\partial_{1x}A_4+\partial_{1y}A_6+\partial_{1z}A_8=0. \tag{2.17}$$

The above equation should match with the continuity equation at $\mathcal{O}(\epsilon^2)$, namely, $\partial_{t2}\delta\rho=0$. Therefore, $A_4=A_6=A_8=0$, and the following three constraints are thus obtained

$$A_4=\left(1-\frac{s_j}{2}\right)j_x^{(1)}+\frac{s_j}{2}j_x^{(eq,1)}+\frac{\delta_t}{2}\Psi_4^{(1)}=0, \tag{2.18a}$$

$$A_6=\left(1-\frac{s_j}{2}\right)j_y^{(1)}+\frac{s_j}{2}j_y^{(eq,1)}+\frac{\delta_t}{2}\Psi_6^{(1)}=0, \tag{2.18b}$$

$$A_8=\left(1-\frac{s_j}{2}\right)j_z^{(1)}+\frac{s_j}{2}j_z^{(eq,1)}+\frac{\delta_t}{2}\Psi_8^{(1)}=0. \tag{2.18c}$$

Eqs. (2.14) and (2.18) together lead to

$$j_x^{(1)}=-F_x^{(1)}\delta_t/2,\quad j_y^{(1)}=-F_y^{(1)}\delta_t/2a,\quad j_z^{(1)}=-F_z^{(1)}\delta_t/2b. \tag{2.19}$$

The next order equilibrium moments $j_{x,y,z}^{(eq,1)}$ and the forcing term $\Psi_{4,6,8}^{(1)}$ are not easily separable since they are coupled in both Eqs. (2.14) and (2.18). However, they

do not appear in our later derivation. For convenience, we can simply set $j_{x,y,z}^{(eq,1)} = 0$, which then leads to $\Psi_4^{(1)} = (1-0.5s_j)F_x^{(1)}$, $\Psi_6^{(1)} = (1-0.5s_j)F_y^{(1)}/a$ and $\Psi_8^{(1)} = (1-0.5s_j)F_z^{(1)}/b$.

Now the 4^{th}, 6^{th} and 8^{th} rows of Eq. (2.8c)

$$\partial_{t2}(\rho_0 u) + \partial_{1x}\left(\frac{A_2}{57} + \frac{A_{10}}{3}\right) + a\partial_{1y}A_{14} + a\partial_{1z}A_{16} = -\frac{s_j}{\delta_t}j_x^{(2)}, \tag{2.20a}$$

$$\partial_{t2}\left(\frac{\rho_0 v}{a}\right) + \partial_{1y}\left(\frac{aA_2}{57} - \frac{aA_{10}}{6} + \frac{aA_{12}}{2}\right) + \partial_{1x}A_{14} + b\partial_{1z}A_{15} = -\frac{s_j}{\delta_t}j_y^{(2)}, \tag{2.20b}$$

$$\partial_{t2}\left(\frac{\rho_0 w}{b}\right) + \partial_{1z}\left(\frac{bA_2}{57} - \frac{bA_{10}}{6} - \frac{bA_{12}}{2}\right) + \partial_{1x}A_{16} + a\partial_{1y}A_{15} = -\frac{s_j}{\delta_t}j_z^{(2)}, \tag{2.20c}$$

are compared to the N-S equations $\mathcal{O}(\epsilon^2)$, namely,

$$\begin{aligned}\partial_{t2}(\rho_0 u) - \partial_{1x}\left[\mu^V \nabla_1 \mathbf{u} + \mu\left(\frac{4}{3}\partial_{1x}u - \frac{2}{3}\partial_{1y}v - \frac{4}{3}\partial_{1z}w\right)\right] \\ -\mu\partial_{1y}\left(\partial_{1y}u + \partial_{1x}v\right) - \mu\partial_{1z}\left(\partial_{1z}u + \partial_{1x}w\right) = 0,\end{aligned} \tag{2.21a}$$

$$\begin{aligned}\partial_{t2}(\rho_0 v) - \partial_{1y}\left[\mu^V \nabla_1 \mathbf{u} + \mu\left(\frac{4}{3}\partial_{1y}v - \frac{2}{3}\partial_{1x}u - \frac{2}{3}\partial_{1z}w\right)\right] \\ -\mu\partial_{1x}\left(\partial_{1y}u + \partial_{1x}v\right) - \mu\partial_{1z}\left(\partial_{1z}v + \partial_{1y}w\right) = 0,\end{aligned} \tag{2.21b}$$

$$\begin{aligned}\partial_{t2}(\rho_0 w) - \partial_{1y}\left[\mu^V \nabla_1 \mathbf{u} + \mu\left(\frac{4}{3}\partial_{1z}w - \frac{2}{3}\partial_{1y}v - \frac{2}{3}\partial_{1x}u\right)\right] \\ -\mu\partial_{1y}\left(\partial_{1y}w + \partial_{1z}v\right) - \mu\partial_{1x}\left(\partial_{1z}u + \partial_{1x}w\right) = 0,\end{aligned} \tag{2.21c}$$

where $\nabla_1 \mathbf{u} \equiv \partial_{1x}u + \partial_{1y}v + \partial_{1z}w$, μ $[kg \cdot m^{-1} \cdot s^{-1}]$ and μ^V $[kg \cdot m^{-1} \cdot s^{-1}]$ are the dynamic shear and bulk viscosity, respectively. In order for Eq. (2.20) to be consistent with Eq. (2.21), we must set $j_x^{(2)} = j_y^{(2)} = j_z^{(2)} = 0$. Furthermore, A_2, A_{10}, A_{12}, A_{14}, A_{15} and A_{16} can be determined in terms of viscosity coefficients and velocity gradients

as

$$A_2 = -\frac{19\mu}{3}\left(\omega_1 + \frac{\omega_2}{a^2} + \frac{\omega_3}{b^2}\right) - 19\kappa_1\mu^V\nabla_1\mathbf{u}, \tag{2.22a}$$

$$A_{10} = -\frac{\mu}{3}\left(2\omega_1 - \frac{\omega_2}{a^2} - \frac{\omega_3}{b^2}\right) - (3-\kappa_1)\,\mu^V\nabla_1\mathbf{u}, \tag{2.22b}$$

$$A_{12} = -\frac{\mu}{3}\left(\frac{\omega_2}{a^2} - \frac{\omega_3}{b^2}\right) - \kappa_2\mu^V\nabla_1\mathbf{u}, \tag{2.22c}$$

$$A_{14} = -\frac{\mu}{a}\left(\partial_{1y}u + \partial_{1x}v\right), \tag{2.22d}$$

$$A_{15} = -\frac{\mu}{ab}\left(\partial_{1y}w + \partial_{1z}v\right), \tag{2.22e}$$

$$A_{16} = -\frac{\mu}{b}\left(\partial_{1z}u + \partial_{1x}w\right), \tag{2.22f}$$

where $\omega_1 = 4\partial_{1x}u - 2\partial_{1y}v - 2\partial_{1z}w$, $\omega_2 = 4\partial_{1y}v - 2\partial_{1x}u - 2\partial_{1z}w$, $\omega_3 = 4\partial_{1z}w - 2\partial_{1y}v - 2\partial_{1x}u$, $\kappa_1 = 1/a^2 + 1/b^2 + 1$ and $\kappa_2 = 1/a^2 - 1/b^2$. Recall that in Eq. (2.15) we defined $\mathbf{A}$ as functions of equilibrium moments $\mathbf{m}^{(eq,1)}$ and non-equilibrium moments $\mathbf{m}^{(1)}$ and the mesoscopic forcing terms $\mathbf{\Psi}$. Re-arranging Eq. (2.8b), $\mathbf{m}^{(1)}$ can be obtained in terms of equilibrium moments and the forcing term as

$$\mathbf{m}^{(1)} = \delta_t\mathbf{S}^{-1}\left[\mathbf{\Psi}^{(1)} - \left(I\partial_{t1} + \hat{C}_\alpha\partial_{1\alpha}\right)\mathbf{m}^{(eq,0)}\right] + \mathbf{m}^{(eq,1)}. \tag{2.23}$$

Substituting Eq. (2.23) into Eq. (2.15), we can express $\mathbf{A}$ as functions of equilibrium moments and forcing components as

$$\mathbf{A} = \delta_t\mathbf{S}^{-1}\mathbf{\Psi}^{(1)} + \mathbf{m}^{(eq,1)} - \left(\mathbf{S}^{-1} - \frac{\mathbf{I}}{2}\right)\left(\mathbf{I}\partial_{t1} + \hat{\mathbf{C}}_\alpha\partial_{1\alpha}\right)\mathbf{m}^{(eq,0)}, \tag{2.24}$$

and it is important to recognize that, from Eq. (2.24), the six components of $m_i^{(eq,1)}$ involved in Eqs. (2.20) and (2.22) are all related to the second-oder moments.

A comparison of Eq. (2.22) and Eq. (2.24) now allows us to design $\mathbf{m}^{(eq)}$ and $\mathbf{\Psi}$ so that the hydrodynamic equations can be satisfied. It is also important to note that the forcing term is introduced to reproduce the macroscopic force, without other impacts on the N-S equations. Therefore, we abide by two basic considerations: (a) all terms that contain macroscopic force $\mathbf{F}$ and mesoscopic forcing terms $\mathbf{\Psi}$ should balance and (b) they should be treated separately. In other words, the model should still work properly if the forcing terms are not present in the LBE and the N-S equations. These

considerations lead to a set of constraints that allow us to derive the most general mesoscopic forcing formulation. The details are presented in Min *et al.* [55] when the general forcing formulations for three D2Q9 models (on both the square and rectangular lattice grids) are considered. The similar inverse design process is conducted here. The final results for our D3Q19 cuboid-grid model based on the above considerations are

$$\begin{cases} q_x^{(0)} = \gamma c^2 \rho_0 u, \\ q_y^{(0)} = \left(a^2\kappa_3 - 4\right) c^2 \rho_0 v/a, \\ q_z^{(0)} = \left(b^2\kappa_3 - 4\right) c^2 \rho_0 w/b, \\ m_x^{(0)} = 0, \\ m_y^{(0)} = 0, \\ m_z^{(0)} = 0, \end{cases} \tag{2.25}$$

$$\begin{cases} \epsilon m_2^{(eq,1)} = \rho_0 \delta_t c^2 \left(h_{11}\partial_x u + h_{12}\partial_y v + h_{13}\partial_z w\right), \\ \epsilon m_{10}^{(eq,1)} = \rho_0 \delta_t c^2 \left(h_{21}\partial_x u + h_{22}\partial_y v + h_{23}\partial_z w\right), \\ \epsilon m_{12}^{(eq,1)} = \rho_0 \delta_t c^2 \left(h_{31}\partial_x u + h_{32}\partial_y v + h_{33}\partial_z w\right), \\ \epsilon m_{14}^{(eq,1)} = \rho_0 \delta_t c^2 \lambda \left(\partial_y u + \partial_x v\right)/a, \\ \epsilon m_{15}^{(eq,1)} = \rho_0 \delta_t c^2 \left[s_c^* \kappa_3 \left(a^2 b^2 - a^2\right)/10 + \lambda\right] \left(\partial_z v + \partial_y w\right)/(ab), \\ \epsilon m_{16}^{(eq,1)} = \rho_0 \delta_t c^2 \left[s_c^* \kappa_3 \left(b^2 - a^2\right)/10 + \lambda\right] \left(\partial_x w + \partial_z u\right)/b, \end{cases} \tag{2.26}$$

where $\kappa_3 = (\gamma + 4)$, $s_e^* = (2 - s_e)/(2s_e)$, $s_n^* = (2 - s_n)/(2s_n)$, and $s_c^* = (2 - s_c)/(2s_c)$. Note that γ is the coefficient in $q_x^{(0)}$, the energy flux in the x direction. In the current model, γ is an adjustable parameter. However, in the MRT LBM model on the cubic lattice, γ is not adjustable [8, 7]. Previously, in several LBM models on a rectangular grid [32, 33, 35, 39, 55], γ is indeed shown to be a free parameter. The coefficients for

other two energy flux moments, $q_y^{(0)}$ and $q_z^{(0)}$, are not free but depend on γ because they are constrained by isotropy requirements, namely, to achieve necessary balance of the transport coefficients associated with different velocity gradients in Eq. (2.22d) to Eq. (2.22f).

It is reminded that the formulations of six $m_i^{(eq,1)}$ moments shown in Eq. (2.25) and (2.26) are derived from the consistency and isotropy considerations with the N-S equations. However, they also bring in additional benefits. For example, λ and h_{ij} are the coefficients in $\epsilon m_i^{(eq,1)}$ as indicated in Eq. (2.25) and (2.26). Some of these coefficients provide a benefit to adjust both shear and bulk viscosity which in this model are given as

$$\mu = \rho_0 \delta_t c^2 \left[\frac{a^2 s_c^* (4+\gamma)}{10} - \lambda \right], \tag{2.27a}$$

$$\mu^V = \rho_0 \delta_t c^2 \left[s_e^* \frac{15(1-\kappa_1 c_s^2) + (4+\gamma)(1+a^2+b^2)}{15\kappa_1} - \frac{h_{11}+h_{12}+h_{13}}{57\kappa_1} \right]. \tag{2.27b}$$

We can conclude from Eq. (2.27) that the relaxation time s_c, s_e are no longer uniquely determined by viscosity since λ and h_{ij} are also adjustable. Therefore, for given physical shear and bulk viscosities, we could set s_c, s_e to any value between 0 and 2. This is not possible in the standard LBM MRT model.

It is also important to note that the expressions of both the shear and bulk viscosities in Eq. (2.27) are consistent with the expressions in the standard D3Q19 MRT LBM with the cubic lattice [8] if we set $a = b = 1$, $\gamma = -2/3$, $\kappa_1 = 3$, and all extended equilibrium moments to zero, namely, $h_{ij} = \lambda = 0$.

The consistency and isotropy considerations specify the value of the coefficients h_{ij} in $\epsilon m_{2,10,12}^{(eq,1)}$ shown in Eq. (2.25) and (2.26). They are determined explicitly as

$$h_{ij} = g_{ij} + \begin{bmatrix} 19 s_e^* \left(\frac{\kappa_3}{5} - \kappa_1 \frac{c_s^2}{c^2} + 1 \right) & 19 s_e^* \left(\frac{a^2 \kappa_3}{5} - \kappa_1 \frac{c_s^2}{c^2} + 1 \right) & 19 s_e^* \left(\frac{b^2 \kappa_3}{5} - \kappa_1 \frac{c_s^2}{c^2} + 1 \right) \\ s_n^* \left(\frac{6-\gamma}{5} - \kappa_3 \frac{c_s^2}{c^2} \right) & s_n^* \left(\frac{a^2 \kappa_3}{10} - \kappa_3 \frac{c_s^2}{c^2} - 1 \right) & s_n^* \left(\frac{b^2 \kappa_3}{10} - \kappa_3 \frac{c_s^2}{c^2} - 1 \right) \\ -s_n^* \kappa_2 \frac{c_s^2}{c^2} & -s_n^* \left(\frac{a^2 \kappa_3}{10} + \kappa_2 \frac{c_s^2}{c^2} - 1 \right) & s_n^* \left(\frac{b^2 \kappa_3}{10} - \kappa_2 \frac{c_s^2}{c^2} - 1 \right) \end{bmatrix}, \tag{2.28}$$

where g_{ij} are calculated as

$$g_{ij} = \frac{1}{\rho_0 \delta_t c^2} \begin{bmatrix} \frac{38(\kappa_1-3)}{3}\mu - 19\kappa_1\mu^V & \frac{38\left(a^2\kappa_1-3\right)}{3a^2}\mu - 19\kappa_1\mu^V & \frac{38\left(b^2\kappa_1-3\right)}{3b^2}\mu - 19\kappa_1\mu^V \\ -\frac{2\kappa_1+6}{3}\mu - \kappa_3\mu^V & \frac{4b^2\kappa_1-6}{3b^2}\mu - \kappa_3\mu^V & \frac{4a^2\kappa_1-6}{3a^2}\mu - \kappa_3\mu^V \\ \frac{2\kappa_2}{3}\mu - \kappa_2\mu^V & -\frac{a^2+2b^2}{a^2b^2}\mu - \kappa_2\mu^V & \frac{2a^2+b^2}{a^2b^2}\mu - \kappa_2\mu^V \end{bmatrix}, \tag{2.29}$$

where $\kappa_1 = 1/a^2 + 1/b^2 + 1, \kappa_2 = 1/a^2 - 1/b^2, \kappa_3 = 2 - 1/a^2 - 1/b^2$. The notation g_{ij} is introduced here only because otherwise the expressions for h_{ij} would be too long to be written within a line. We find that h_{ij} are functions of the aspect ratios a and b, shear and bulk viscosities μ and μ^V, relaxation parameters s_e, and s_n, sound speed c_s, and γ. The expressions for h_{ij} are derived based on the requirements in Eq. (2.22) and they work together to achieve two goals:

1. There could be three shear viscosity coefficients and three bulk viscosity coefficients in Eq. (2.22a)(2.22b)(2.22c) and these viscosity coefficients would be different in different directions if we set $h_{ij} = 0$, as shown clearly in [33] for some 2D rectangular-grid models. Thus, h_{ij} are used to achieve the isotropy conditions, namely, all shear viscosity coefficients are constrained to a same value, and all bulk viscosity coefficients are made identical. This was our original motivation of extending the equilibrium moments as in Eq. (2.7b).

2. After the key model parameters, a, b, μ, μ^V, s_e, s_n, c_s, and γ are chosen, we can always find a solution for h_{ij} such that Eq. (2.22) holds true and shear (and bulk) viscosity are consistent in different equations.

2.3 Summary of the Cuboid Lattice Model

We shall now summarize the derived model details that are needed to implement the model. First, the equilibrium moments at both the leading order and the next order

are summarized as

$$\mathbf{m}^{(eq)} = \begin{bmatrix} \delta\rho \\ \delta\rho\left(19\kappa_1 c_s^2 - 30\right) + 19\rho_0\left(u^2 + \frac{v^2}{a^2} + \frac{w^2}{b^2}\right), \\ \varepsilon^{(eq,0)} \\ \rho_0 u \\ \gamma c^2 \rho_0 u \\ \rho_0 v/a \\ \frac{a^2\kappa_3 - 4}{a} c^2 \rho_0 v \\ \rho_0 w/b \\ \frac{b^2\kappa_3 - 4}{b} c^2 \rho_0 w \\ \delta\rho\kappa_3 c_s^2 + \rho_0\left(2u^2 - \frac{v^2}{a^2} - \frac{w^2}{b^2}\right) \\ \pi_{xx}^{(eq,0)} \\ \delta\rho\kappa_2 c_s^2 + \rho_0\left(\frac{v^2}{a^2} - \frac{w^2}{b^2}\right) \\ \pi_{ww}^{(eq,0)} \\ \rho_0 uv/a \\ \rho_0 uw/b \\ \rho_0 vw/ab \\ 0 \\ 0 \\ 0 \end{bmatrix} + \rho_0\delta_t c^2 \begin{bmatrix} 0 \\ h_{11}\partial_x u + h_{12}\partial_y v + h_{13}\partial_z w \\ 0 \\ 0 \\ 0 \\ 0 \\ 0 \\ 0 \\ h_{21}\partial_x u + h_{22}\partial_y v + h_{23}\partial_z w \\ 0 \\ h_{31}\partial_x u + h_{32}\partial_y v + h_{33}\partial_z w \\ 0 \\ \lambda\left(\partial_y u + \partial_x v\right)/a \\ \left[\frac{a^2 s_c^* \kappa_3\left(b^2-1\right)}{10} + \lambda\right]\frac{\partial_z v + \partial_y w}{ab} \\ \left[\frac{s_c^* \kappa_3\left(b^2-a^2\right)}{10} + \lambda\right]\frac{\partial_x w + \partial_z u}{b} \\ 0 \\ 0 \\ 0 \end{bmatrix}, \tag{2.30}$$

$$\epsilon j_x^{(1)} = -F_x\delta_t/2, \quad \epsilon j_y^{(1)} = -F_y\delta_t/2a. \quad \epsilon j_z^{(1)} = -F_y\delta_t/2b. \tag{2.31}$$

where the first array on the right represents the equilibrium moments at the leading order $\mathbf{m}^{(eq,0)}$, the second array on the right represents the equilibrium moments

at the next order $\mathbf{m}^{(eq,1)}$, namely, the extended equilibrium moments. As before, $\kappa_1 = 1/a^2 + 1/b^2 + 1, \kappa_2 = 1/a^2 - 1/b^2, \kappa_3 = 2 - 1/a^2 - 1/b^2$, $s_e^* = (2 - s_e)/2s_e, s_n^* = (2 - s_n)/2s_n, s_c^* = (2 - s_c)/2s_c$. The essential key adjustable parameters are γ, λ, h_{ij} and c_s^2. The coefficients h_{ij} are defined by Eq. (2.28) and (2.29). Furthermore, $\varepsilon^{(eq,0)}, \pi_{xx}^{(eq,0)}$ and $\pi_{ww}^{(eq,0)}$ are not constrained by the N-S equations, therefore, theoretically they can be set to any value. Usually we choose $\varepsilon^{(eq,0)} = \alpha c^4 \delta\rho + \beta\rho_0 c^2 (u^2 + v^2), \pi_{xx}^{(eq,0)} = \omega_{xx} c^2 p_{xx}^{(eq,0)}, \pi_{ww}^{(eq,0)} = \omega_{ww} c^2 p_{ww}^{(eq,0)}$, where the values of $\alpha, \beta, \omega_{xx}, \omega_{ww}$ could be determined through a linear stability analysis [8, 7]. Other extended equilibrium moments and forcing terms in Eq. (2.30) that are not constrained by the N-S equations are simply set to zero for simplicity. The potential use of these terms as a way to optimize numerical stability of the current model can be a topic of investigation in the future.

It is also important to note that the cuboid model would reduce to the standard D3Q19 MRT LBM indicated in [8] when both aspect ratios a and b are set to 1, and the equilibrium moments are not extended, namely, $h_{ij} = \lambda = 0$. Also, the exact definitions of all equilibrium moments in [8] could be recovered from Eq. (2.30).

Our derivation shows that $m_1^{(1)} = \Psi_1^{(1)} = 0$, thus the presence of forcing does not affect the local density fluctuation and the calculation of pressure is not affected. Also, according to the multi-scale expansion in Eq. (2.7a), $m_4 = j_x^{(0)} + \epsilon j_x^{(1)} = \rho_0 u - F_x \delta_t/2$. Therefore, the computation of hydrodynamic velocity is affected by the forcing, *i.e.*, $\rho_0 u = \mathbf{M}_{4i} f_i + F_x \delta_t/2$. The same applies to the velocity in the y and z direction. Therefore, the pressure and velocity in this model should be calculated according to

$$p = \delta\rho c_s^2, \tag{2.32a}$$

$$u = (f_i e_{ix} + F_x \delta_t/2)/\rho_0, \tag{2.32b}$$

$$v = (f_i e_{iy} + F_y \delta_t/2)/\rho_0, \tag{2.32c}$$

$$w = (f_i e_{iz} + F_z \delta_t/2)/\rho_0. \tag{2.32d}$$

where e_i is the discrete particle velocity given by Eq. (2.1), and e_{ix}, e_{iy}, e_{iz} represents the x, y and z component of e_i, respectively. Putting all the above results together for

the forcing term, we have

$$\boldsymbol{\Psi} = \epsilon\boldsymbol{\Psi}^{(1)} = \begin{bmatrix} 0 \\ 38(1-0.5s_e)(uF_x + vF_y/a^2 + wF_z/b^2) \\ \Psi_3 \\ (1-0.5s_j)F_x \\ \Psi_5 \\ (1-0.5s_j)F_y/a \\ \Psi_7 \\ (1-0.5s_j)F_z/b \\ \Psi_9 \\ 2(1-0.5s_n)(2uF_x - vF_y/a^2 - wF_z/b^2) \\ \Psi_{11} \\ 2(1-0.5s_n)(vF_y/a^2 - wF_z/b^2) \\ \Psi_{13} \\ (1-0.5s_c)(vF_x + uF_y)/a \\ (1-0.5s_c)(vF_x + uF_y)/ab \\ (1-0.5s_c)(vF_x + uF_y)/b \\ \Psi_{17} \\ \Psi_{18} \\ \Psi_{19} \end{bmatrix}. \tag{2.33}$$

A few observations about the mesoscopic forcing term can now be made: (1) The components of the mesoscopic forcing term are related to macroscopic forcing field $\mathbf{F} = (F_x, F_y, F_z)$, macroscopic velocity, and relaxation parameters. The mesoscopic forcing terms $\boldsymbol{\Psi}$ are added to Eq. (2.2) as $\boldsymbol{\Phi} = \mathbf{M}^{-1}\boldsymbol{\Psi}\delta_t$ to realize the effect of macroscopic forcing at the mesoscopic level; (2) nine of the 19 components: Ψ_3, Ψ_5, Ψ_7, Ψ_9, Ψ_{11},

Ψ_{13}, Ψ_{17}, Ψ_{18}, and Ψ_{19}, are not constrained by the N-S equations and thus they can be specified *freely*. Basically, only the components associated with 0^{th}, 1^{st}, and 2^{nd} order moments are determined by the continuity and N-S equations. This flexibility could be used to potentially improve the numerical stability, namely, we can design the nine irrelevant components in the forcing term to enhance numerical stability.

The above completes the description of the MRT LBM model details on a cuboid lattice, with a general nonuniform forcing. We should now provide a few general comments on how to use this model in a typical application of solving a 3D viscous flow. First, all physical parameters of a flow problem are gathered, namely, viscosity coefficients μ and μ^V, macroscopic forcing field $\mathbf{F}$, domain size, and the initial condition and boundary conditions of the flow, *etc.*. They determine the length scale L, characteristic velocity U_0, and the flow Reynolds number. Next, key parameters of the cuboid model and numerical settings are specified, including grid aspect ratios a and b, speed of sound c_s, the coefficient in the $x-$component energy flux γ, relaxation parameters $\mathbf{S}$. In the proposed cuboid model, in principle, the relaxation parameters can be set to any value between 0 and 2 as long as the code is stable, because enough degrees of freedom are introduced so the relaxation parameters are not uniquely related to the physical viscosity coefficients. The parameter λ is then calculated according to Eq. (2.27a). With Eqs. (2.28) and (2.29), h_{ij} are then determined from μ, μ^V, a, b, c_s, relaxation parameters, and γ. Thus, all equilibrium moments $\mathbf{m}^{(eq)}$ can now be specified using Eq. (2.30). The mesoscopic forcing term $\mathbf{\Psi}$ is also known from Eq. (2.33). Therefore, we could evolve the flow step by step according to the lattice Boltzmann equation, Eq. (2.2). In the cuboid model, the additional equilibrium moments $\epsilon\mathbf{m}^{(eq,1)}$ contain strain-rate components. Thus, we need to compute them every time step. These strain-rate components can be calculated from the non-equilibrium moments so they all have a second-order accuracy. The method of calculating strain-rate components is given in the Appendix.

Chapter 3

NUMERICAL VALIDATIONS OF THE PROPOSED CUBOID LATTICE MODEL

In this section, the D3Q19 MRT lattice Boltzmann method on a cuboid lattice grid derived in Sec. 2 will be validated using three different benchmark cases: the transient laminar channel flow, the three-dimensional decaying Taylor-Green vortex flow, and the turbulent channel flow. Furthermore, the order of numerical accuracy of this model will be examined.

3.1 Transient Laminar Channel Flow

First, we use the two-dimensional, transient, laminar channel flow to validate the cuboid model as the analytical solution for this time-dependent flow is available. The laminar channel flow is a wall-bounded flow with two parallel flat walls. In the simulation, the mid-link bounce back scheme is applied to fulfill the no-slip boundary condition. The wall boundary is placed half lattice away from the boundary fluid nodes. On each link cutting the wall, the inward post-streaming non-equilibrium distribution of a boundary node is set to the pre-streaming distribution in the opposite direction, namely, $f_{\bar{i}}\left(\mathbf{x}_B, t+\delta_t\right) = \tilde{f}_i\left(\mathbf{x}_B, t\right)$ where $\mathbf{x}_B$ is the location of a boundary node, $\tilde{f}_i$ represents the post-collision (pre-streaming) distribution function with particle velocity e_i, which points into the wall. $f_{\bar{i}}$ represents the post-streaming distribution function in the direction opposite to e_i.

The domain is three-dimensional, with periodic boundary conditions in both the streamwise and the spanwise directions. In the code, x, y, and z represent the transverse, streamwise, and spanwise direction, respectively. All simulation results from the cuboid D3Q19 model are compared to the analytical solution.

In Table 3.1, the parameter settings of the cuboid model with four different aspect ratios are listed. In the most extreme case, the aspect ratio $a = \delta_y/\delta_x = \delta_{streamwise}/\delta_{transverse}$ and $b = \delta_z/\delta_x = \delta_{spanwise}/\delta_{transverse}$ are set to 20, thus the lattice in this case looks like a square plate. The channel height H of all cases is set to $H = 40\delta_{transverse}$. Since the flow is laminar, there is no variation in *streamwise* and *spanwise* directions. We only need to resolve the flow in the *transverse* direction and in time. The computational domain size for all cases is set to $N_x \times N_y \times N_z = 40 \times 2 \times 2$. The maximum streamwise velocity V_{max} is set to 0.1 and the speed of sound c_s is set to 0.6325 so the maximum Mach number is much smaller than 1/3. The kinematic shear and bulk viscosities are set to 0.1333 so the steady-state Reynolds number $Re = V_{max}H/\nu$ is 30. The adjustable parameter γ depends on the aspect ratio as this parameter was found to affects the numerical stability of the cuboid model. For all cases, all relaxation parameters in Eq. (2.5) are set to 1.2.

The flow starts from rest, and a uniform and constant body force F_y $[kg{\cdot}m^{-2}{\cdot}s^{-2}]$ is applied in the streamwise direction to drive the flow to its steady state with the long-time maximum velocity V_{max} at the channel centerline. The external body force F_y according to the steady-state solution is

$$F_y = \frac{8\rho_0\nu V_{max}}{H^2}. \tag{3.1}$$

On the developing stage, the theoretical solution of velocity for the laminar channel flow could be solved by separation of variables. The result is given as

$$\frac{v_{theory}}{V_{max}} = \sum_{n=1}^{\infty} \frac{32}{k_n^3}\left[1 - exp\left(-\frac{k_n^2\nu t}{H^2}\right)\right] sin\left[\frac{k_n\,(x-0.5)}{H}\right], \tag{3.2}$$

where $k_n = (2n-1)\pi$. t is the physical time of the flow, which is the current time step in the simulation. In the above equation, x represents the coordinate of a specified point. Thus $(x - 0.5)$ is the position of this point in the physical space since the physical position is located at the center of lattice, which is half grid from the boundary. In the simulation, it is impossible to sum infinite terms to get the theoretical solution of velocity. Therefore, only 300 terms are summed in our simulation, which is quite enough according to our test.

Table 3.1: Parameter settings of the laminar channel flow with cuboid lattice grids.

Cases	Aspect ratio	H	V_{max}	ν	ν^V	c_s	γ	Re
1	$a = b = 2$	40	0.1	0.1333	0.1333	0.6325	-3.0	30
2	$a = b = 4$	40	0.1	0.1333	0.1333	0.6325	-3.8	30
3	$a = b = 10$	40	0.1	0.1333	0.1333	0.6325	-3.97	30
4	$a = b = 20$	40	0.1	0.1333	0.1333	0.6325	-3.98	30

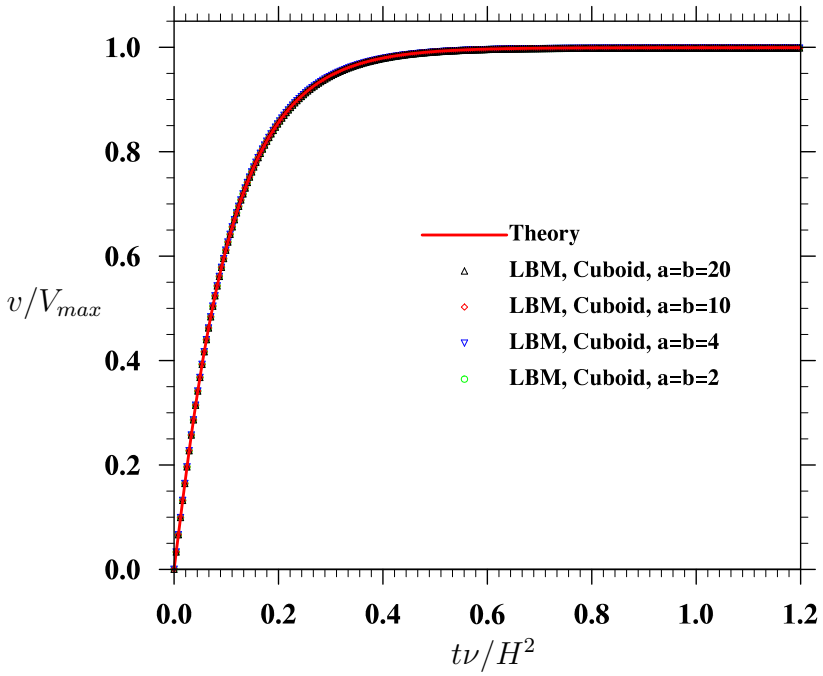

Figure 3.1: The time evolution of the streamwise velocity v at $x/H = 0.4875$ (close to the channel centerline). All quantities are normalized as indicated.

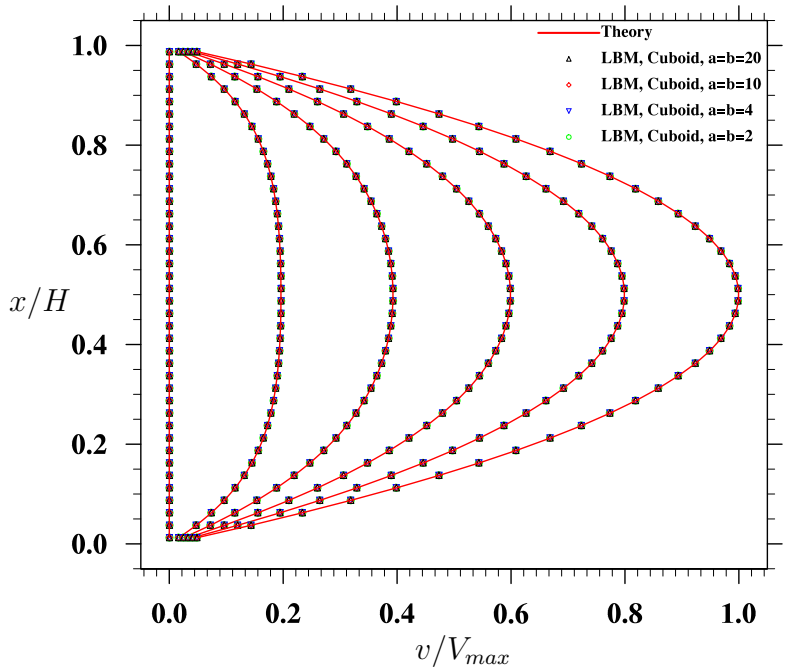

Figure 3.2: The streamwise velocity profiles at six different times, $t\nu/H^2 = 0, 0.0248, 0.0537, 0.0958, 0.166$, and 1.24. All quantities are normalized as indicated.

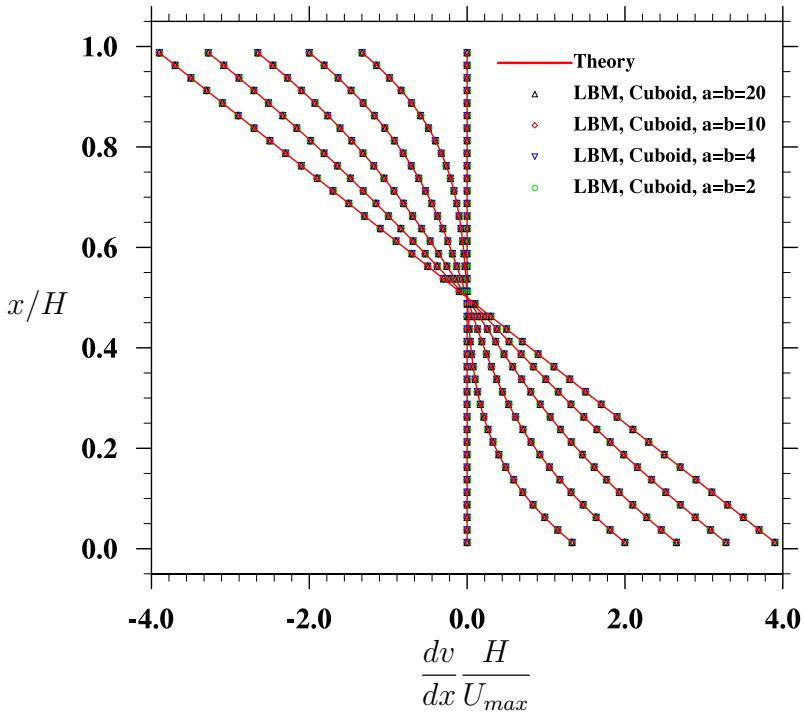

Figure 3.3: The profiles of velocity gradient dv/dx at six different times, $t\nu/H^2 = 0, 0.0248, 0.0537, 0.0958, 0.166$, and 1.24. All quantities are normalized as indicated.

In Fig. (3.1), the time evolution of the streamwise velocity v at $x/H = 0.4875$ is shown for all cases. The theoretical velocity at this location is also plotted as the benchmark. Under the constant uniform external force, the streamwise velocity increases with time. The steady-state velocity is reached at roughly $t\nu/H^2 = 0.5$ (see Fig. 3.1), when the the external force is balanced by the viscous shear stress. Since the location we selected is $x/H = 0.4875$, which is very close to the center of channel, the ratio v/V_{max} at the steady state is very close to one. Results from all aspect ratios are in excellent agreement with the theory at all times.

In Figs. (3.2) and (3.3), the streamwise velocity profiles and the profiles of velocity gradient dv/dx are shown, respectively. There are six different curves in the plots and they represent the profiles at six different times: $t\nu/H^2 = 0, 0.0248, 0.0537, 0.0958, 0.166, 1.24$, respectively. All results are compared to the theoretical velocity profiles at the corresponding time and again an excellent agreement is observed, regardless of the aspect ratios used.

3.2 3D Decaying Taylor-Green Vortex Flow

The 3D Taylor-Green vortex flow was proposed by Taylor and Green [56] to study the production of small eddies from large eddies. They solved the three-dimensional time-dependent flow analytically using a short-time perturbation expansion, making this an ideal benchmark for any 3D numerical method. In the 3D Taylor-Green flow, the kinetic energy of the flow decreases in time, and at the same time, is transferred from the initial large-scale eddy to newly-created small-scale eddies. The energy-cascading feature is not present in the 2-D Taylor-Green vortex flow [33] often used to validate numerical methods in 2D. We have also solved the 3D Taylor-Green vortex flow by a highly-accurate pseudo-spectral method. Both the short-time analytical solution and the spectral solution will be used to validate the present cuboid-lattice model.

Specifically, we consider the 3D Taylor-Green vortex flow with the following

initial velocity field

$$\begin{cases} u = U_0 cos\,(2\pi x/L)\, sin\,(2\pi y/L)\, sin\,(2\pi z/L)\,, \\ v = -U_0 sin\,(2\pi x/L)\, cos\,(2\pi y/L)\, sin\,(2\pi z/L)\,, \\ w = 0, \end{cases} \tag{3.3}$$

where u, v and w represent the velocity in the x, y, z directions, respectively. U_0 is the characteristic velocity of the flow at the initial time. The domain size is L, which is the same in the three directions. Periodic boundary condition is assumed in all three directions.

Taylor and Green [56] obtained the short-time perturbation solution as follows. First, a Poisson equation of the pressure could be derived by combining the continuity equation with the N-S equations. Based on the initial velocity given in Eq. (3.3), the pressure field could be solved from the Poisson equation. Next, the pressure is then substituted back to the N-S equations to determine the time derivative of velocity at the initial time, which can be integrated to obtain the first approximation of the short-time solution. The above process (velocity - pressure - time derivative of velocity - new velocity) is regarded as one perturbation iteration. Then, the new velocity field becomes the starting solution for the next iteration. After a few iterations, the short-time theoretical solution of the 3D Taylor-Green vortex flow can be obtained, with the time dependence expressed through mode coefficients as polynomials in time. The final three-dimensional time-dependent perturbation solution of the velocity field, the average kinetic energy, and the average dissipation rate are presented in [56]. Some key parameter settings of this flow are listed in Table 3.2. The aspect ratio of the cuboid lattice is set to $a = \delta_y/\delta_x = 0.8$ and $b = \delta_z/\delta_x = 0.8$. The domain size L is set to $L_x = L_y = L_z = 64$ and 128, respectively. The number of lattices in each direction is chosen according to the aspect ratio $a = \delta_y/\delta_x$ and $b = \delta_z/\delta_x$ to keep the physical domain size identical. Since the flow is decaying, Re_0 represents the initial Reynolds number defined as $Re_0 = 2\pi U_0 L/\nu$. In this test case, results of cuboid model are compared with results of the corresponding MRT-LBM with cubic lattice and spectral

Table 3.2: Parameter settings of the 3D decaying Taylor-Green vortex flow.

Cases	Aspect ratio	L	$N_x \times N_y \times N_z$	Re_0	U_0	ν	ν^V	c_s^2	γ
1	$a = b = 0.8$	64	$64 \times 80 \times 80$	300	0.10186	0.0035	0.0035	0.3	-1.5
2	$a = b = 0.8$	128	$128 \times 256 \times 128$	300	0.05093	0.0035	0.0035	0.3	-2.0

method. The relaxation parameter of both cases are set to $s_e = 0.8, s_\varepsilon = 0.6, s_q = 0.8, s_n = 0.8, s_c = 0.8, s_\pi = 0.8, s_m = 1.95$ to obtain a better stability. The results of cuboid model are compared with results of the corresponding MRT-LBM with cubic lattice and spectral method.

Four statistics of the flow are calculated and compared to the results of other models and the short-time theory, the average kinetic energy $E = \langle \mathbf{u}_i^2 \rangle / 2$, averaged total dissipation rate $D = 2\nu \langle (S_{ij} - \nabla \cdot \mathbf{u} \delta_{ij}/3)^2 + \nu^V (\nabla \cdot \mathbf{u})^2 \rangle$, where S_{ij} is the strain rate, ν^V is the bulk viscosity and $\nabla \cdot \mathbf{u}$ is the divergence. The effect of bulk viscosity is considered since the usual LBM simulation is not fully incompressible so the divergence of the flow is not strictly zero. If the flow is fully incompressible, then the total dissipation rate would reduce to $D = 2\nu \langle S_{ij}^2 \rangle$. The velocity skewness $S_\mathbf{u}$ and flatness $F_\mathbf{u}$ are calculated. The velocity skewness and flatness are defined as

$$S_\mathbf{u} = \frac{\left\langle \frac{1}{3} \left[(\partial_x u)^3 + (\partial_y v)^3 + (\partial_z w)^3 \right] \right\rangle}{\left\langle \frac{1}{3} \left[(\partial_x u)^2 + (\partial_y v)^2 + (\partial_z w)^2 \right] \right\rangle^{3/2}}, \tag{3.4a}$$

$$F_\mathbf{u} = \frac{\left\langle \frac{1}{3} \left[(\partial_x u)^4 + (\partial_y v)^4 + (\partial_z w)^4 \right] \right\rangle}{\left\langle \frac{1}{3} \left[(\partial_x u)^2 + (\partial_y v)^2 + (\partial_z w)^2 \right] \right\rangle^2}, \tag{3.4b}$$

where S_u and F_u represent the velocity skewness and flatness, respectively. The velocity skewness and flatness are high order statistics and thus could be used to evaluate the accuracy of the small scale structure of the simulation.

From Fig. 3.4 to Fig. 3.5, the results of two cuboid cases are compared to the corresponding MRT-LBM with cubic lattice, and spectral method, and the theoretical solution of 3D Taylor-Green vortex flow. On the one hand, it is proved by examining the resolution parameter $k_{max}\eta$ that the flow could be well resolved in the spectral method with a 128^3 of grids [57, 58], where $k_{max} = L/3$ is the spectral truncation

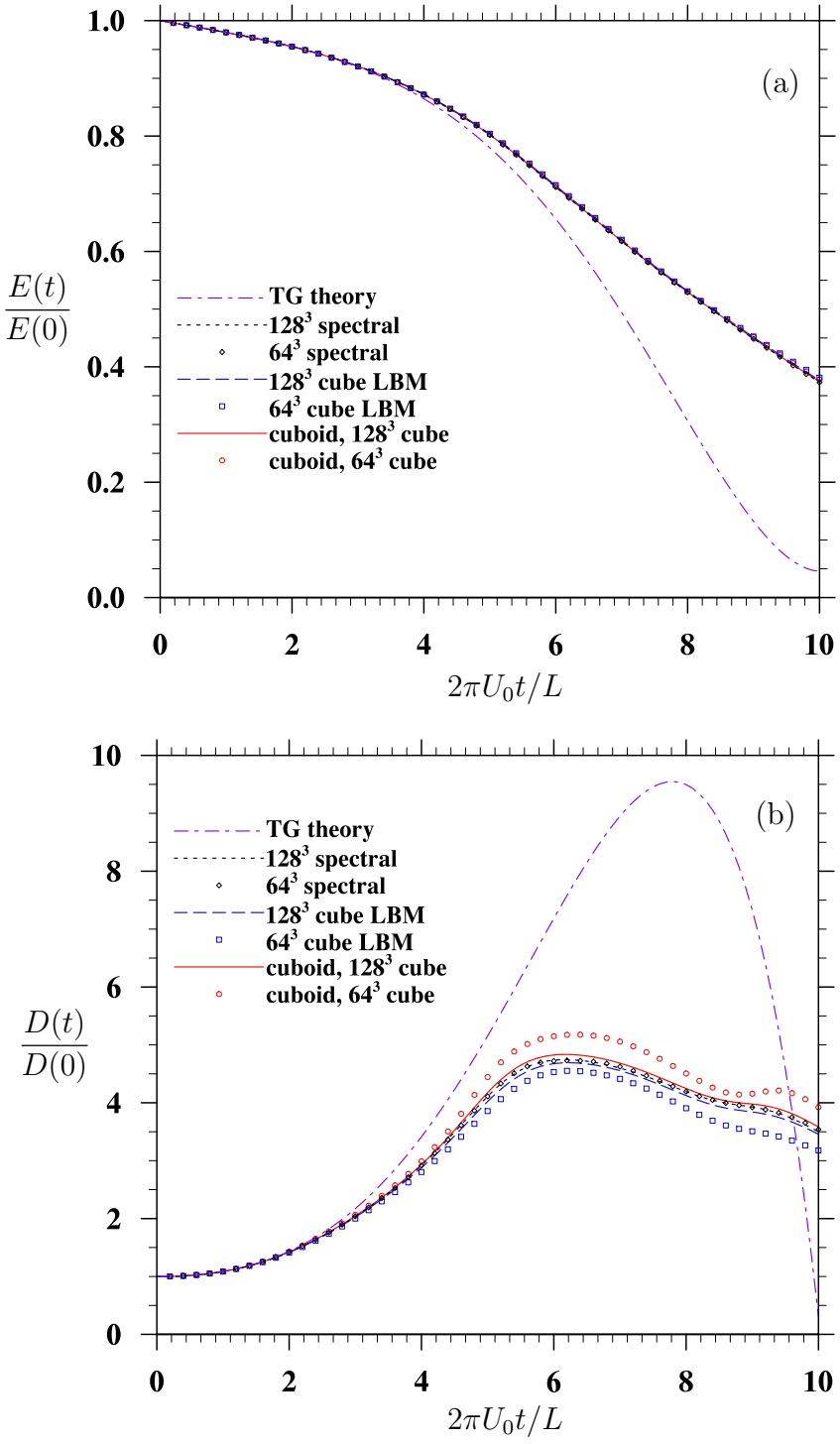

Figure 3.4: The time evolutions of (a) the average kinetic energy E_k, (b) the average dissipation rate ϵ. The results of two cuboid cases in Table 3.2 are compared to those of the two MRT-LBM cases with the cubic lattice and two different resolutions, the spectral method, and the short-time theory.

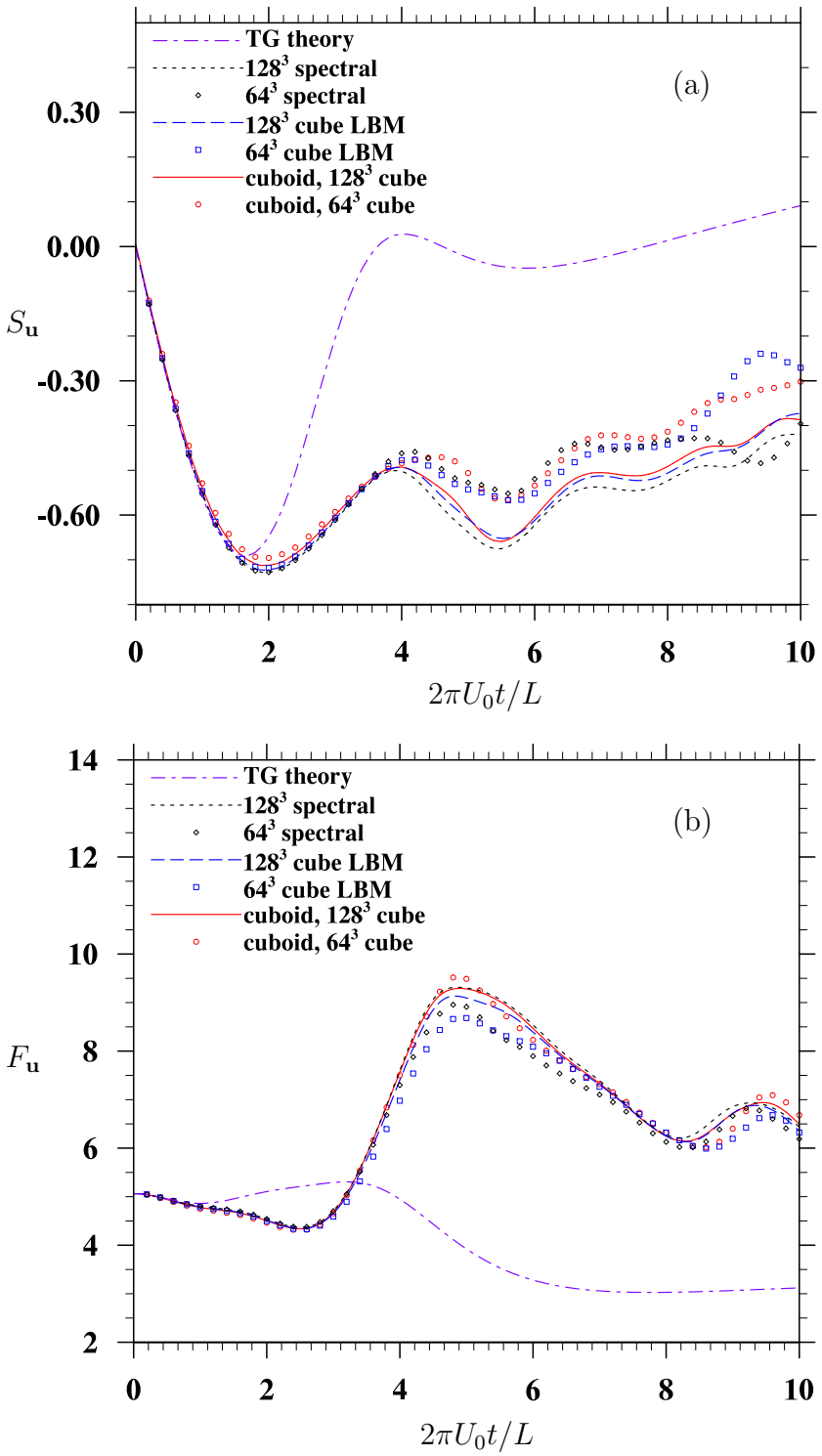

Figure 3.5: The time evolutions of (a) the velocity-derivative skewness, and (b) the velocity-derivative flatness. The results of two cuboid cases in Table 3.2 are compared to those of the two MRT-LBM cases with the cubic lattice and two different resolutions, the spectral method, and the short-time theory.

radius in the spectral method, L is the domain size and η is the Kolmogorov length. On the other hand, in the spectral method, the combination of second-order time integration accuracy and spectral accuracy in space yields an overall order of accuracy that is higher than two. Meanwhile, LBM is a second-order accurate method as proved in [45]. Thus, the 128^3 spectral method is used as the benchmark case since it is the most accurate one among all test cases and the flow is well resolved in this case.

In Fig. (3.4) and Fig. (3.5), all curves are matched at the beginning, including the short-time theory of the Taylor-Green vortex flow. But the theoretical solutions of 3D Taylor-Green vortex flow are only valid for a short time. For low order statistics like kinetic energy and dissipation rate, the short-time theory is valid for about 2 non-dimensional time. For higher order statistics like velocity skewness, the theory of 3D Taylor-Green vortex flow is valid for about 1.5 non-dimensional time and the lifetime of theoretical velocity flatness is less than 1.

In the first plot of Fig. (3.4), the kinetic energy decays monotonically. The time evolution of normalized kinetic energy of all models are matched with a good agreement, which means the large structure is adequately captured by all models with two different resolutions. Meanwhile, the result of high resolution cases is slightly better than low resolution cases comparing to the 128^3 spectral method, which is expected. The second plot of Fig. (3.4) shows the time evolution of the normalized dissipation rate of the flow. The results from all models are identical until two non-dimensional times, which is expected since all simulations are initialized with the same profile and there are only large flow structures in the initial field so the flow is well resolved at the beginning of all cases. As indicated in [56], small-scale flow structure like small eddies will be created from large eddies. Therefore, to fully resolve the flow, the number of lattice grids should also be increased. For a quantity like dissipation rate which is related to the small-scale structure of the flow, it is easy to tell that the result of 128^3 cubic and cuboid LBM is much better than the corresponding 64^3 cases. Different from the evolution of kinetic energy, the dissipation of the flow first increases due to the production of small-scale structure and then decreases since the flow is decaying

and the Reynolds number is reducing.

Fig. 3.5 shows the time evolution of the velocity-derivative skewness and flatness of different models. Recall that in Fig. 3.4, the difference of kinetic energy between different resolutions are small. Here we observe that all high resolution cases are significantly better than low resolution cases comparing to the 128^3 spectral method. This is because the velocity-derivative skewness and flatness are high-order quantities and are more sensitive to the fluid motion at small scales. The above results mean that 64^3 is not enough to fully resolve the flow. Another reason of the discrepancy between different models is that the system is highly non-linear. Therefore, a small error would increases rapidly over time and leads to a different local structure. If the time of simulation is long enough, even the whole domain would be affected by the difference of local flow structures. For example, the results of two spectral simulations at different resolutions are only matched till 3.5 non-dimensional times. Therefore, results of the proposed cuboid lattice model are still reasonable comparing to the spectral method and the LB models with cubic lattice.

In Fig. 3.6, the velocity profiles on the line $x/L = 1/4, y = z$, at the non-dimensional time $2\pi U_0 t/L = 5$, is plotted for the cuboid case 1 in Table 3.2 and a MRT-LBM with 64^3 cubic lattices. The velocity profiles of two models are matched exactly. The velocity profiles at other times and on some other lines are also examined (but not shown here), and in all cases the results of the cuboid model are in excellent agreement with MRT-LBM results on a cubic lattice.

In summary, the D3Q19 MRT lattice Boltzmann model with a cuboid lattice presented in this paper has been validated by simulating the laminar channel flow and a 3D decaying Taylor-Green vortex flow. All results of the cuboid model are compared to the analytical solutions or results from other models, showing a good agreement with corresponding benchmark data from spectral simulation or analytical solutions.

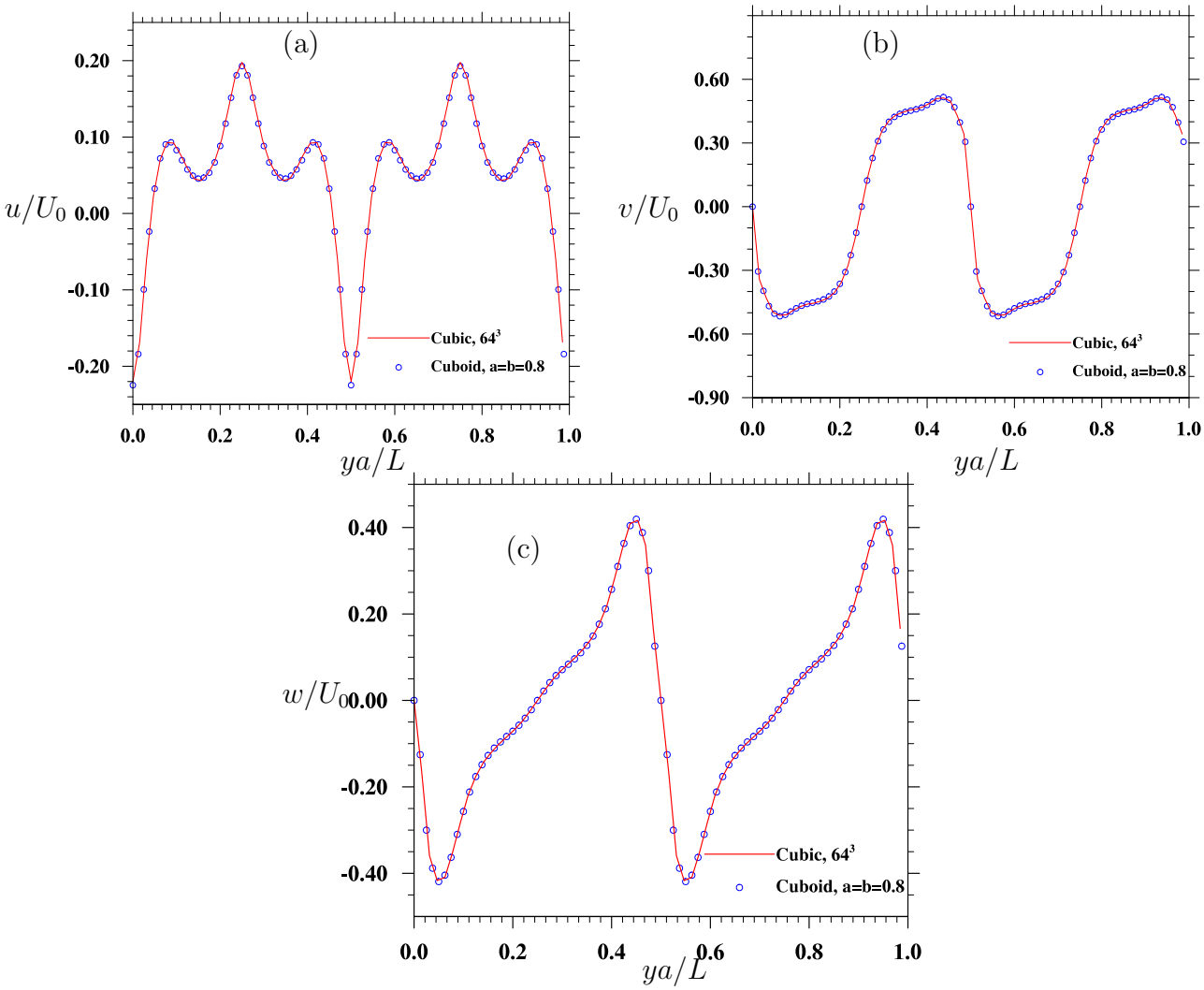

Figure 3.6: The velocity profiles on a line $x/L = 1/4$ and $y = z$ at the non-dimensional time $2\pi U_0 t/L = 5$. (a) Velocity in the x direction, (b) velocity in the y direction, and (c) velocity in the z direction. Results of the cuboid model are compared to results of the corresponding MRT-LBM with 64^3 cubic lattice. All quantities are normalized as indicated.

3.3 Single Phase Turbulent Channel Flow

The final test case is the turbulent channel flow, which is a canonical wall-bounded turbulent flow [26, 59, 60]. This is a time-dependent and three-dimensional flow. The flow is also highly inhomogeneous and anisotropic, especially in the near-wall region. Like the laminar channel flow, the turbulent channel flow is also bounded by two parallel flat walls. Again, x, y, and z represent the transverse, streamwise, and spanwise direction, respectively. At a sufficiently high flow Reynolds number, the flow may transit from a laminar flow to a turbulent flow. In this paper, we only focus on the fully developed stage of turbulent channel flow which have been documented extensively, both in terms of direct numerical simulations and experimental measurements [26, 61, 62].

In this first simulation of a turbulent channel flow using the cuboid model, the domain size is set to $2H \times 4H \times 2H$, where H here is the channel *half* width. Although this domain is not very wide in the streamwise and spanwise directions, reasonable flow statistics can still be obtained as shown in our previous studies of particle-laden turbulent channel flows [63]. The periodic boundary condition is applied to both the streamwise (y) direction and the spanwise (z) direction. In the transverse (x) direction, again the mid-link bounce back (as described in Sec. 3.1) is applied to satisfy the no-slip boundary condition. In this simulation, 2D domain decomposition [20] is used to parallelize the code, and an efficient one-step two-array approach is used to integrate the collision and streaming sub-steps.

The simulation of turbulent channel flow could be divided into three stages:

1. The initial excitation of turbulent fluctuations. Starting from an initial flow field, a non-uniform time-dependent perturbation force field is applied to the flow, in addition to the physical constant body force, to promote and accelerate velocity fluctuations in the flow.

2. Rapid transition to turbulent flow. Once velocity fluctuations in all the three directions have reached a certain level, the perturbation force field is then switched

off. The constant body force can now sustain the turbulent fluctuations and the flow gradually evolves to a fully developed turbulent channel flow.

3. The fully developed turbulent channel flow. At this stage, the flow is statistically stationary, although the local flow structures continue to evolve in time. A simulation over a sufficiently long period of time can then be used to obtain average flow statistics such as the mean and turbulent r.m.s. velocity profiles.

In this simulation, the perturbation force is applied for 3 eddy turnover times. The eddy turnover time is defined as H/u_τ, where the friction velocity is $u_\tau = \sqrt{\tau_w/\rho_0}$, and τ_w is the average wall shear stress. The friction Reynolds number $Re_\tau = u_\tau H/\nu$ is set to 180, where ν is the kinematic shear viscosity. The wall length unit is defined as $\delta_\tau = \nu/u_\tau$. All quantities with superscript + are normalized by u_τ and δ_τ. The values of key parameters used for the turbulent channel flow are listed in Table 3.3. The two aspect ratios are set to $a = \delta_y/\delta_x = 1.25$ and $b = \delta_z/\delta_x = 1$, and $\delta_x = 1$ in lattice units. The half channel width H is set to $100\delta_x$. The domain size is $2H \times 4H \times 2H$, Since $\delta_y/\delta_x = 1.25$, thus for the same physical domain size the number of lattice nodes in the streamwise direction is 80% of the number used in the standard LBM model using the cubic lattice. Namely, the grid resolution for the cuboid lattice is $199 \times 320 \times 200$, compared to $199 \times 400 \times 200$ in the cubic lattice model [63].

The kinematic shear viscosity ν was set to 0.0036. The bulk viscosity ν^V is set to 0.1 to help maintain the numerical stability. This leads to a frictional velocity $u_\tau = 0.00648$. All relaxation parameters in Eq. (2.5) are set to 1.2. When simulating the turbulent channel flow with the cuboid model, we found that the numerical instability could occur for larger lattice aspect ratio. The reason for the numerical instability and methods to enhance numerical stability of the cuboid model should be studied in the future.

In Fig. (3.7a), the streamwise velocity v averaged over the whole domain is shown as a function of time. The result from the standard LBM model with the cubic lattice (taken from Wang *et al,* [63]), using the same physical parameters, initial

Table 3.3: Parameter settings of the turbulent channel flow.

Aspect ratio	Re_τ	H	Domain size	N_x, N_y, N_z	ν	ν^V	u_τ	c_s	γ
$a = 1.25, b = 1$	180	100	$2H, 4H, 2H$	$199, 320, 200$	0.0036	0.1	0.00648	0.6325	-0.8

flow field, and perturbation forcing is shown for comparison. The time evolutions of the averaged streamwise velocity based on the two models are identical for about 1.5 eddy turnover times. Then they become different at a given time due to inherent nonlinearity. Nevertheless, the evolutions remain similar qualitatively. Both reach the stationary stage after about 40 to 60 eddy turnover times. Thus, the statistic from 63 to 117.7 eddy turnover times are used to calculate the mean profiles at the stationary stage. The mean velocity averaged over $63 < tu_\tau/H < 117.7$ is 15.57 based on the cuboid model, compared to 15.67 from the cubic model. Both are within 0.5% of the value of 15.63 based on the spectral method [61]. All averaged profiles to be shown below are obtained time-averaging over the time interval of $63 < tu_\tau/H < 117.7$.

The mean streamwise-velocity profiles are compared in Fig. 3.7(b), where x^+ is the distance from the channel wall in wall units. At a given x, the streamwise velocity is averaged over the $y - z$ plane. Only the profiles over half of the channel are shown since they are symmetric. The linear viscous sublayer and the logarithmic region can be clearly identified. The result from the cuboid model is in excellent agreement with that from the cubic model, and they both agree with the spectral benchmark data taken from the literature [61, 62, 64, 65] except that the streamwise velocity of the proposed cuboid lattice model is slightly smaller than other models near the center of channel.

The corresponding profiles for the averaged Reynolds stress $-\langle u'v'\rangle/u_\tau^2$ are shown in Fig. 3.8(a), and these of root-mean-square (r.m.s.) fluctuation velocities are presented in Fig. 3.8(b). The results of the cuboid model are compared with the results from the standard cubic-lattice model and spectral benchmark data. Clearly, the cuboid model reproduces the same statistics and profiles of the cubic model. They

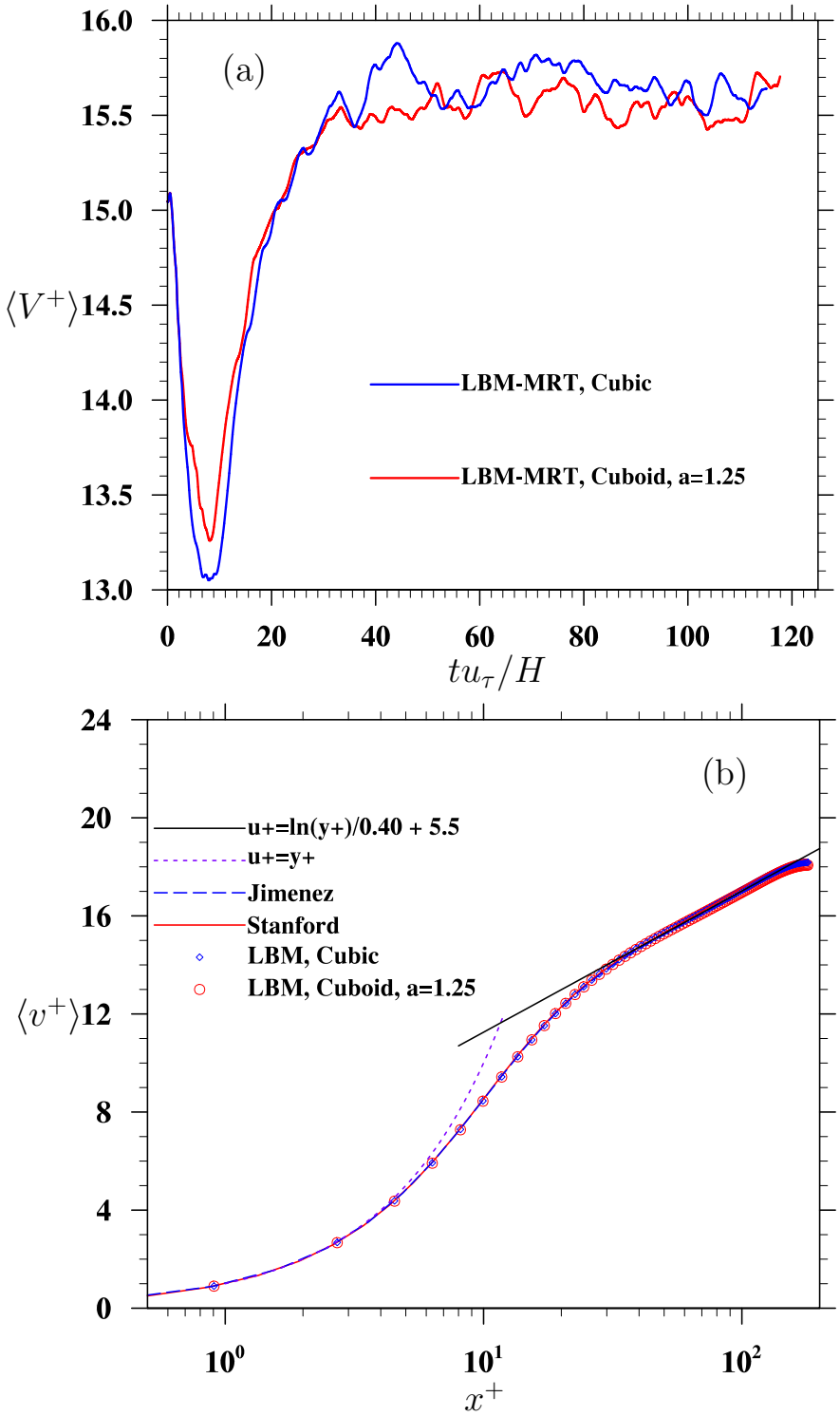

Figure 3.7: (a) The streamwise velocity averaged over the whole domain when the flow reaches the stationary stage. (b) Profiles of mean streamwise velocity as a function of x^+ when the flow reaches the stationary stage. All quantities are normalized as indicated.

both are in reasonable agreement with the spectral benchmark data. There are also some differences in the streamwise and spanwise r.m.s. velocity profiles, which is related to the use of different domain size as discussed in Wang *et al.* [63, 66].

In summary, the cuboid lattice model is used to simulate the fully developed turbulent channel flow. The statistics of the fully developed flow are compared with the results from the cubic-lattice model in [63, 66] and previous spectral simulation data. All results are in good agreement. For the same physical domain size, the cuboid-lattice model with $\delta_y = 1.25\delta_x$ uses 20% less grid points in the streamwise direction when compared to the cubic-lattice model. With proper optimization of model parameters, we believe that larger aspect ratios could be used to further reduce the computational cost.

3.4 The Order of Accuracy of the Cuboid Model

It has been known that the lattice Boltzmann method has a second-order accuracy in space and time [33, 39, 45]. The order of accuracy of the proposed cuboid model can be examined using the results for the transient laminar channel flow and the 3D decaying Taylor-Green vortex flow presented in Sec. 3.1 and 3.2. To examine the accuracy with the laminar channel flow, we use Case 2 in Table 3.1 ($a = b = 4$) with four different grid resolutions: $10\times2\times2$, $20\times4\times4$, $40\times8\times8$, and $80\times16\times16$. Other parameters are the same as in Table 3.1 and all results are compared to the theoretical solution. To study the accuracy with 3D Taylor-Green vortex flow, we choose Case 1 in Table 3.2 (a = b = 0.8) with 5 different resolutions: $32\times40\times40$, $64\times80\times80$, $128\times160\times160$, $256\times320\times320$, and $512 \times 640 \times 640$. Due to the anisotropy of lattice sizes of the cuboid model, it is impossible to match the node points in the cuboid model with other models like the spectral method based on the cubic grid. The short-time theory of 3D Taylor-Green flow could be a great benchmark tool for average statistics like the average kinetic energy, but it is only valid at short times. However, the order of accuracy must be based on local errors at the exact same locations. Therefore, we instead use the results of the cuboid model at $512\times640\times640$ as the benchmark when computing local errors for the

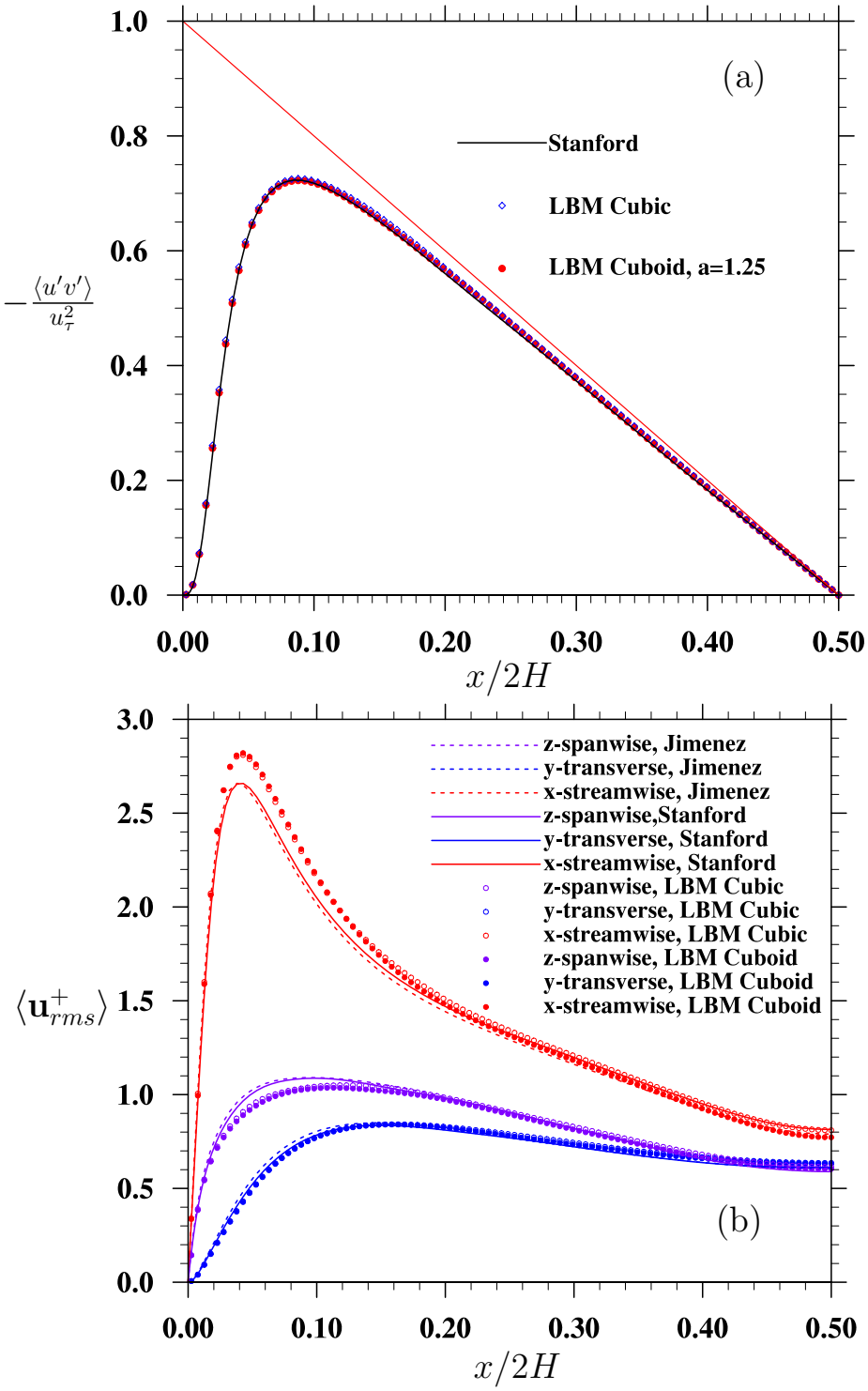

Figure 3.8: (a) The Reynolds stress $-\langle u'v' \rangle / u_\tau^2$ profiles and (b) the r.m.s. velocity profiles. All quantities are normalized as indicated.

other 4 lower resolutions. Using the results of the cuboid grid at the highest-resolution as a benchmark has another benefit, namely, the initial flow conditions are identical at the mesoscopic level due to the same initialization method used.

In order to measure the order of accuracy, the $L1$ and $L2$ errors are calculated as

$$\epsilon_{L1}(t) = \frac{\sum_{x,y,z} |q_n(x,y,z,t) - q_b(x,y,z,t)|}{\sum_{x,y,z} |q_b(x,y,z,t)|}, \tag{3.5a}$$

$$\epsilon_{L2}(t) = \frac{\sqrt{\sum_{x,y,z} |q_n(x,y,z,t) - q_b(x,y,z,t)|^2}}{\sqrt{\sum_{x,y,z} |q_b(x,y,z,t)|^2}}. \tag{3.5b}$$

where $q_n(x,y,z,t)$ and $q_b(x,y,z,t)$ represent the numerical value and corresponding benchmark value of a quantity at location (x,y,z) and time t. For each quantity, the $L1$ and $L2$ error norms for velocity at different grid resolutions are calculated according to Eq. (3.5). The order of accuracy could be estimated based on either $L1$ or $L2$ error norms. Assume the error norm calculated from one given resolution is $\epsilon_0(t)$, as we increase the resolution by a factor of m in each direction, the new error norm should be smaller and is denoted by $\epsilon_m(t)$. Then the order of accuracy n is estimated as

$$n(t) = log_m \left(\frac{\epsilon_0(t)}{\epsilon_m(t)} \right). \tag{3.6}$$

The order of accuracy is first checked by laminar flow at $t\nu/H^2 = 1$. Only the streamwise velocity v are examined because the other two velocity components are always zero in the laminar channel flow. The results are compiled in Table 3.4, showing that the order of accuracy is between 1.6 to 1.8. That is because the laminar channel flow can be easily well resolved. Thus, increasing the grid resolution has a less significant effect on the error norm especially when the resolution is already high enough.

For the case of the 3D decaying Taylor-Green vortex flow, the results of error norms computed from each velocity component are compiled in Table 3.5 and Table 3.8, for L_1 and L_2 error norm at two different times, $2\pi U_0 t/L = 3$ and 5, respectively. The results clearly demonstrated that the order of accuracy is around 2. In addition,

Table 3.4: The order of accuracy of the cuboid model evaluated with results from the transient laminar channel flow. The theoretical solutions are used as the benchmark. Results are calculated at $t\nu/H^2 = 1$. The streamwise velocity v is examined.

Resolutions	$v\,(L1)$	order	$v\,(L2)$	order
$10 \times 2 \times 2$	1.658E-2	$(-)$	1.521E-2	$(-)$
$20 \times 4 \times 4$	4.577E-3	1.857	4.183E-3	1.862
$40 \times 8 \times 8$	1.354E-3	1.757	1.236E-3	1.759
$80 \times 16 \times 16$	4.426E-4	1.613	4.040E-4	1.613
Averaged		1.742		1.745

Table 3.5: The L_1 error norm and the order of accuracy of the cuboid model evaluated with the 3D decaying Taylor-Green vortex flow. Results of the cuboid model with a resolution of $512 \times 640 \times 640$ are used as the benchmark to compute the error norms of the cuboid model at lower grid resolutions. Results are calculated at $2\pi U_0 t/L = 3$.

Resolutions	$u/v/w\,(L1)$	order $u/v/w$
$32 \times 40 \times 40$	2.805E-2 / 2.263E-2 / 4.009E-2	$(-)$
$64 \times 80 \times 80$	6.162E-3 / 4.309E-3 / 8.224E-3	2.187 / 2.393 / 2.286
$128 \times 160 \times 160$	1.172E-3 / 8.336E-4 / 1.583E-3	2.394 / 2.370 / 2.377
$256 \times 320 \times 320$	2.352E-4 / 2.101E-4 / 3.224E-4	2.317 / 1.988 / 2.287
Averaged		2.299 / 2.250 / 2.316

Table 3.6: The L_2 error norm and the order of accuracy of the cuboid model evaluated with the 3D decaying Taylor-Green vortex flow. Results of the cuboid model with a resolution of $512 \times 640 \times 640$ are used as the benchmark to compute the error norms of the cuboid model at lower grid resolutions. Results are calculated at $2\pi U_0 t/L = 3$.

Resolutions	$u/v/w\,(L2)$	order $u/v/w$
$32 \times 40 \times 40$	3.439E-2 / 2.458E-2 / 4.336E-2	$(-)$
$64 \times 80 \times 80$	7.242E-3 / 4.881E-3 / 9.262E-3	2.248 / 2.332 / 2.227
$128 \times 160 \times 160$	1.356E-3 / 1.010E-3 / 1.904E-3	2.417 / 2.273 / 2.282
$256 \times 320 \times 320$	2.541E-4 / 2.341E-4 / 3.930E-4	2.416 / 2.109 / 2.276
Averaged		2.360 / 2.238 / 2.262

Table 3.7: The L_1 error norm and the order of accuracy of the cuboid model evaluated with the 3D decaying Taylor-Green vortex flow. Results of the cuboid model with a resolution of $512 \times 640 \times 640$ are used as the benchmark to compute the error norms of the cuboid model at lower grid resolutions. Results are calculated at $2\pi U_0 t/L = 5$.

Resolutions	$u/v/w\,(L1)$	order $u/v/w$
$32 \times 40 \times 40$	1.001E-1 / 1.043E-1 / 1.128E-1	$(-)$
$64 \times 80 \times 80$	2.104E-2 / 2.005E-2 / 2.485E-2	2.250 / 2.379 / 2.182
$128 \times 160 \times 160$	4.143E-3 / 3.279E-3 / 4.641E-3	2.344 / 2.612 / 2.422
$256 \times 320 \times 320$	6.619E-4 / 5.503E-4 / 8.162E-4	2.646 / 2.575 / 2.508
Averaged		2.413/2.522/2.370

Table 3.8: The L_2 error norm and the order of accuracy of the cuboid model evaluated with the 3D decaying Taylor-Green vortex flow. Results of the cuboid model with a resolution of $512 \times 640 \times 640$ are used as the benchmark to compute the error norms of the cuboid model at lower grid resolutions. Results are calculated at $2\pi U_0 t/L = 5$.

Resolutions	$u/v/w\,(L2)$	order $u/v/w$
$32 \times 40 \times 40$	1.261E-1 / 1.239E-1 / 1.210E-1	$(-)$
$64 \times 80 \times 80$	2.969E-2 / 2.876E-2 / 3.465E-2	2.087 / 2.107 / 1.804
$128 \times 160 \times 160$	6.044E-3 / 5.222E-3 / 6.706E-3	2.296 / 2.461 / 2.369
$256 \times 320 \times 320$	1.049E-3 / 8.904E-4 / 1.237E-3	2.526 / 2.552 / 2.439
Averaged		2.303 / 2.373 / 2.204

the $L1$ and $L2$ error norms with different aspect ratios are also compared to study if the error norms are dependent on the aspect ratio. Four laminar flow cases listed in Table 3.1 are used at the same resolution of $40 \times 2 \times 2$. The $L1$ and $L2$ error norms of streamwise velocity v are compared in Fig. 3.9. We can conclude that, in this case, the error norms are independent of the aspect ratio since all curves essentially overlap with one another.

3.5 Summary

In this chapter, the D3Q19 multiple-relaxation time lattice Boltzmann cuboid model is validated by three different benchmark cases: the transient laminar channel flow, the 3D energy-cascading Taylor-Green vortex flow and the single phase turbulent channel flow.

Firstly, In the simulation of laminar channel flow, four different aspect ratios of the cuboid lattice grid are tested, namely, $a = b = 2$, $a = b = 4$, $a = b = 10$, $a = b = 20$, where $a = \delta_y/\delta_x$, and $b = \delta_z/\delta_x$ represents the ratio of lattice length in different directions. In the most extreme case where both a and b are set to 20, the shape of the cuboid lattice is like a plate. Thus, the number of lattice in the wall normal direction (transverse direction) of the channel is much larger than the streamwise direction and the spanwise direction so that the wall normal direction is fully resolved and the number of nodes on the other two directions could be greatly reduced since the flow is homogeneous in the streamwise and spanwise directions of the laminar channel flow. The velocity profiles and the strain rate profiles obtained by the proposed cuboid model agree well with the theoretical solutions of the laminar channel flow. All results are matched perfectly.

Then, the cuboid model is validated by the 3D energy-cascading Taylor-Green vortex flow. This flow is a non-homogeneous anisotropic flow with energy being transferred from the large scales to the small scales, which makes it a better benchmark case than the previous laminar channel flow to validate the cuboid lattice model. The 3D Taylor-Green vortex flow could be solved analytically by using the perturbation theory

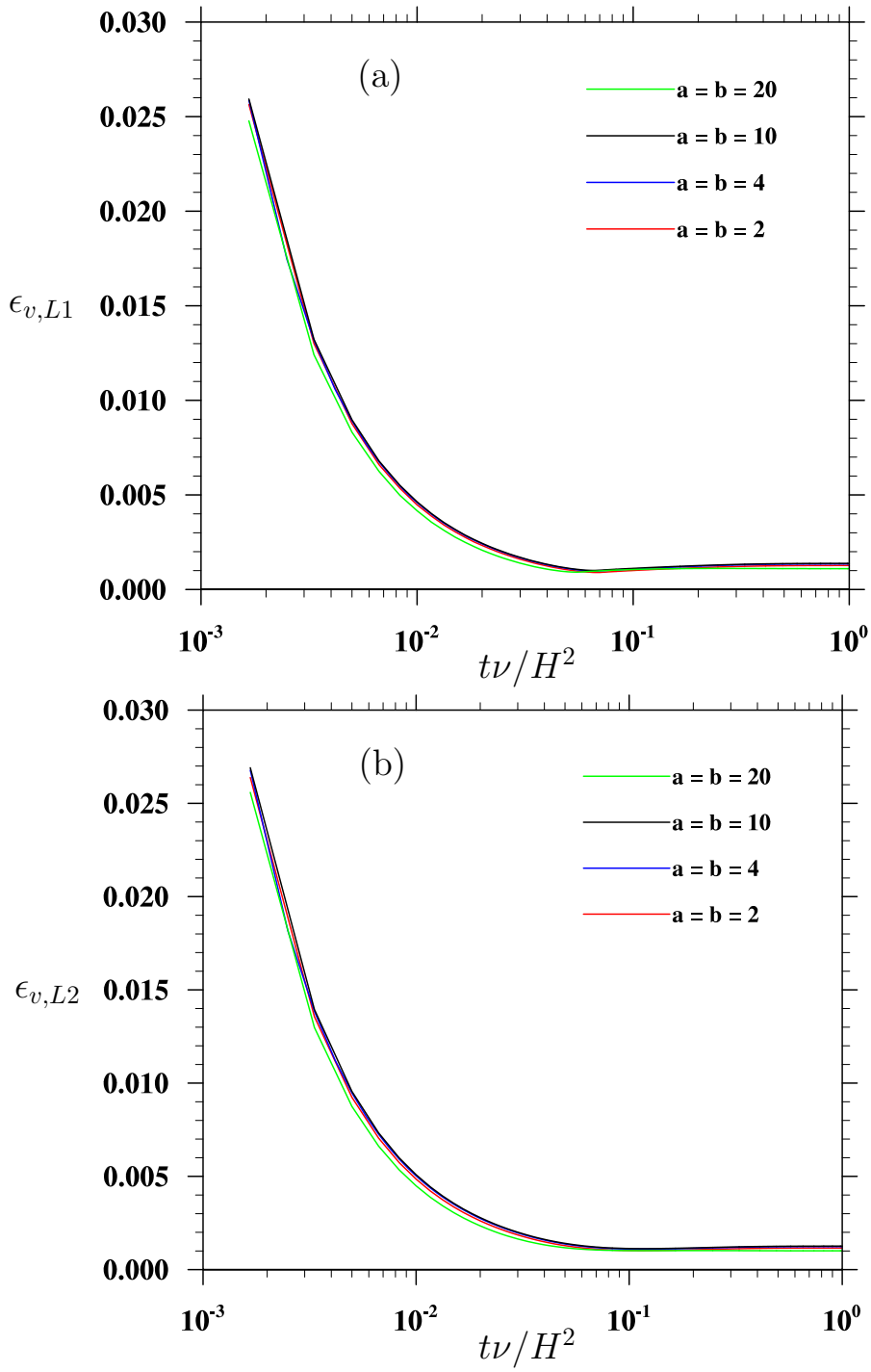

Figure 3.9: (a) The $L1$ error norm and (b) the $L2$ error norm of the streamwise velocity v in the laminar channel flow simulations. Results from four different aspect ratios are compared.

and solving the Poisson equation of pressure [56], but the theoretical solution of the 3D Taylor-Green vortex flow is only valid for a short time. Four different flow statistics are calculated, namely, the kinetic energy, dissipation rate, velocity-derivative skewness and flatness. The result of the cuboid model are compared to the spectral method and the D3Q19 MRT LBM with cubic lattice gird. The results of cuboid model are in a good agreement with the spectral benchmark data. In addition, we found that 64^3 is not enough to fully resolve the 3D Taylor-Green vortex flow especially when more small eddies are created during the evolution of the flow.

The fully-developed turbulent channel flow is the third benchmark case to validate the cuboid lattice model. In this case, a constant body force is applied to drive the flow, and a time-dependent perturbation force is added to excite the turbulence. The flow statistic is averaged over a time interval after the flow is fully developed. The velocity profile, Reynolds stress profile and root-mean-square (RMS) velocity profiles of the cuboid model are calculated and compared to the results of spectral method and the MRT lattice Boltzmann method on a cubic lattice. All results are in excellent agreement.

Finally, we examined the order of accuracy of the cuboid model by computing the $L1$ and $L2$ error norms of velocity in the laminar channel flow and the 3D Taylor-Green vortex flow. In the laminar channel flow, the numerical velocity are compared to the short-time analytical solution. The results shows that the cuboid lattice LBM model is about 1.7 order accurate. In the 3D Taylor-Green vortex flow, the theoretical solution of the flow is only valid for a short time so it cannot be used as the benchmark to calculate the error norm. Therefore, a cuboid case with a resolution of $512\times640\times640$ is used as the benchmark to check the error of other low resolution cases. Based on the result of 3D Taylor-Green vortex flow, the cuboid lattice model is second order accurate. In the laminar channel flow, the error norm of four cases with different aspect ratios are compared and they are close to each other. Thus, at least in a linear flow like laminar channel flow, increasing the aspect ratio would not lead to the deterioration of result.

Chapter 4

CONCLUSION AND FUTURE WORKS

4.1 Summary and Conclusions

In this thesis, a D3Q19 multiple-relaxation time lattice Boltzmann model on a cuboid lattice grid has been developed through an inverse design analysis based on the multiscale Chapman-Enskog expansion. In this cuboid model, the lattice grid-lengths in the three spatial directions could be set to different values, namely, the aspect ratios a and b, defined as $a = \delta_y/\delta_x$, $b = \delta_z/\delta_x$, are input parameters of the cuboid model, where δ_x, δ_y and δ_z are the grid sizes in the three directions, respectively. In the model, the equilibrium moments are extended to include additional higher-order terms in order to address the anisotropy problem of viscosity coefficients resulting from the use of the cuboid lattice. This extension allows the proposed cuboid model to adopt the same transformation matrix of the standard cubic model between the particle distributions and physical moments. A mesoscopic forcing term is also added to the lattice Boltzmann equation to realize the effect of macroscopic time-dependent and spatially non-uniform forcing.

To recover the correct hydrodynamic equations, the Chapman-Enskog expansion has been used to develop all constraints for the cuboid model. These constraints are then applied to design the leading-order and higher-order equilibrium moments, and mesoscopic forcing terms. This inverse design process ensures a consistent and general cuboid model.

Based on the inverse design analysis shown in Chapter 2, 16 of the 19 leading-order equilibrium moments, 6 of the 19 higher-order equilibrium moments, and 10 of the 19 mesoscopic forcing terms can be determined directly from the constraints

resulting from the hydrodynamic equations. Clearly, further studies are needed to optimize those *free* terms that are not constrained by the hydrodynamic equations, in order to achieve a better numerical stability. It is also found that the higher-order equilibrium moments offer two functions: (i) to resolve the anisotropy of viscosity coefficients associated with the use of the anisotropic lattice structure, and (ii) to adjust both shear and bulk viscosities independent of the relaxation parameters. By construction, the higher-order equilibrium moments affect the stress components of the hydrodynamic flow.

The cuboid model is then validated by three different benchmark cases, namely, the transient laminar channel flow, the 3D energy-cascading Taylor-Green vortex flow, and the fully developed turbulent channel flow.

Firstly, the proposed cuboid model is validated by a transient laminar channel flow. The highest aspect ratios of the cuboid lattice grid is set to $a = \delta_y/\delta_x = 20$, and $b = \delta_z/\delta_x = 20$. As a validation, the velocity and the strain rate profiles of the proposed cuboid lattice model are compared with the theoretical solutions of the laminar channel flow. All results are in perfect agreement. The second numerical validation is the 3D energy-cascading Taylor-Green vortex flow. In this flow, a short-time theoretical solution could be obtained by using the perturbation theory and solving the Poisson equation for pressure [56]. Additionally, while the flow is decaying, the energy will be transferred from the large-scale structure to the small-scale structures, which makes the 3D Taylor-Green vortex flow highly anisotropic, non-homogeneous and non-linear. In summary, the 3D Taylor-Green vortex flow is a great benchmark case to examine the proposed cuboid lattice model. The kinetic energy, dissipation rate, velocity-derivative skewness and flatness of the cuboid model are calculated and compared to the spectral method and the D3Q19 MRT LBM on a cubic lattice. The results of cuboid model are in good agreement with the benchmark data from either the short-time analytical solution or spectral simulations. The third benchmark case is the fully-developed turbulent channel flow. A time-dependent, non-uniform perturbation force is applied to excite the turbulence. All flow statistics are calculated and averaged over a time

interval after the flow is fully developed. The results of the proposed cuboid lattice model are in an excellent agreement with the spectral method and the MRT lattice Boltzmann method with a cubic lattice.

Finally, the order of accuracy of the cuboid model is examined via the $L1$ and $L2$ error norms. Two numerical cases are used to measure the order of accuracy, namely, the transient laminar channel flow and the 3D Taylor-Green vortex flow. In the laminar channel flow, the numerical results are compare to the theory, while in the 3D Taylor-Green vortex flow, the theoretical solution of the flow is only valid for a short time so it cannot be used as the benchmark to calculate the error norm. Therefore, a cuboid case with a resolution of $512 \times 640 \times 640$ is used as the benchmark to compute the error of accuracy for other low resolution cases. Based on our results, the proposed cuboid lattice model is indeed a second order scheme.

With the proposed cuboid-lattice model, a smaller number of lattice points can be used to achieve the same result for an anisotropic flow such as the turbulent channel flow. This is because, compared to the standard cubic lattice, a relatively coarser lattice grid can be used in the direction where the flow variables vary more gradually ($i.e.$, , the streamwise direction of a channel or pipe). Thus, the overall computational efficiency can be improved. In a simple flow like laminar channel flow, the performance of the proposed cuboid model is excellent. When some some complex flows such as turbulent channel flow and 3D Taylor-Green flow are considered, the cuboid lattice model suffers from the trouble of instability. Additional stability analysis are required to improve the stability of the proposed cuboid lattice model.

4.2 Future Works

The initial motivation of developing a lattice Boltzmann model with a cuboid lattice is to reduce amount of lattice grids so that a relatively coarser lattice grid can be used in the direction where the flow variables vary more gradually, and the simulation will be more computational efficient. For this purpose, it is desired to have arbitrary aspect ratios, a and b. According to the derivation of the proposed cuboid

lattice model in Chapter 2, the aspect ratio of the lattice could be set to any value and a correct Navier-Stokes equation can always be recovered. However, this is not true in the real simulation and the code became numerically unstable. In the simulation of laminar channel flow, the aspect ratio of the lattice grid could be easily raised to $a = \delta_y/\delta_x = 20$ and $b = \delta_z/\delta_x = 20$ so the lattice is very anisotropic and the code is still stable. However, in the simulation of turbulent channel flow and 3D Taylor-Green vortex flow, the aspect ratio can currently only be varied from 0.8 to 1.25 due to the complexity of flow structure.

In this thesis, no analysis has been performed to understand the numerical instability, and use such to optimize the free parameters. Through a literature survey, several alternative ways to improve the stability of LBM could be found. The first way is to apply the linear stability analysis [7, 67, 68, 69], in which the lattice Boltzmann equation is linearized by representing the distribution function or moment as a mean part and a perturbation part. The value of adjustable parameters are optimized through a von Neumann analysis [67, 70]. The second alternative method is the selective viscosity filtering [70] which damps out unphysical instabilities by adding different filtering approaches. Thirdly, the viscosity counteracting approach [71, 72] should be studied as well. In the viscosity counteracting approach, an extra viscosity is added to the original one to increase the apparent viscosity in high Reynolds number simulation, by correcting the added viscosity using an external forcing term [71, 72].

Our main remaining task is to find out the origin of instability for our proposed cuboid model by performing the linear stability analysis [7, 67, 68, 69]. Or enhance the stability of the proposed cuboid lattice model by using other methods mentioned above [70, 71, 72].

BIBLIOGRAPHY

[1] U. Frisch, B. Hasslacher, and Y. Pomeau, Lattice-Gas Automata for the Navier-Stokes Equation, Phys. Rev. Lett. 56, 1505 (1986).

[2] Y. H. Qian, D. dHumi‘eres and P. Lallemand, Lattice BGK Models for Navier-Stokes Equation, Europhys. Lett., 17 (6), pp. 479–484 (1992).

[3] X. He and L.-S. Luo, A priori derivation of the lattice Boltzmann equation, Phys. Rev. E, 55, R6333 (1997);

[4] X. He, L.-S. Luo, Theory of the lattice Boltzmann method: From the Boltzmann equation to the lattice Boltzmann equation, Phys. Rev. E, 56 (1997) 6811.

[5] S. Chen, G. D. Doolen, Lattice Boltzmann method for fluid flows, Annual Review of Fluid Mechanics 30 (1) (1998) 329-364.

[6] S. Succi, The Lattice-Boltzmann Equation, Oxford University Press, Oxford, 2001.

[7] Lallemand P., Luo L.S., Theory of the lattice Boltzmann method: Dispersion, dissipation, isotropy, Galilean invariance, and stability, Phys. Rev. E, 61 (2000) 6546.

[8] D. dHumi‘eres, I. Ginzburg, M. Karfczyk, *et al.* , Multiple-relaxation-time lattice Boltzmann models in three dimensions, Phil. Trans. R. Soc. Lond. A (2002) 360, 437–451.

[9] P. Lallemand, L.-S. Luo, Theory of the lattice Boltzmann method: Acoustic and thermal properties in two and three dimensions, Phys. Rev. E, 68, 036706 (2003).

[10] L.-S. Luo, W. Liao, X. W. Chen, Y. Peng, W. Zhang, Numerics of the lattice Boltzmann method: Effects of collision models on the lattice Boltzmann simulations, Phys. Rev. E 83, 056710 (2011)

[11] Wang L., Guo Z., Shi B., Zheng C.,Evaluation of three lattice Boltzmann models for particulate flows, Comm. Compt. Phys., 13 (2013): 1151–1172.

[12] Mei R., Luo L.-S., Shyy W., An Accurate Curved Boundary Treatment in the Lattice Boltzmann Method, J. Comp. Phys., 155, 307–330 (1999).

[13] Mei R., Shyy W., Yu D., Luo L.-S., Lattice Boltzmann Method for 3-D Flows with Curved Boundary, J. Comp. Phys., 161, 680–699 (2000).

[14] Guo Z.-L., Zheng C. G., Shi B. C., An extrapolation method for boundary conditions in lattice Boltzmann method, Phys. of fluids, 14, 2007 (2002).

[15] P. Lallemand, L.-S. Luo, Lattice Boltzmann method for moving boundaries, J. Comp. Phys., 184 (2003) 406–421.

[16] Z. Guo, C. Shu, Lattice Boltzmann method and its applications in engineering (advances in computational fluid dynamics),World Scientific Publishing Company, 2013.

[17] S. Succi, I. Karlin, H. Chen, Colloquium: Role of the H theorem in lattice Boltzmann hydrodynamic simulations, Rev. Mod. Phys. 74, 1203 (2002).

[18] D. Yu, R. Mei, L.-S. Luo, W. Shyy, Viscous flow computations with the method of lattice Boltzmann equation, Prog. Aerosp. Sci. 39, 329 (2003).

[19] L-P. Wang, B. Afsharpoya, Modeling fluid flow in fuel cells using the lattice Boltzmann approach, Mathematics & Computers in Simulation, 72 (2006) 242–248.

[20] H. Gao, C. Q. Qiu, D. Fan, Y. Jin, L-P. Wang, 2010, Three-dimensional microscale flow simulation and colloid transport modeling in saturated soil porous media, Comp.& Math. Appl., 59 (2010): 2271–2289.

[21] Pan C. X. , Luo L.-S., Miller C. T., An evaluation of lattice Boltzmann schemes for porous medium flow simulation,Computers & Fluids 35 (2006) 898–909.

[22] L-P. Wang, O. Ayala, H. Gao, *et al.* , Study of forced turbulence and its modulation by finite-size solid particles using the lattice Boltzmann approach, Comp.& Math. Appl., 67 (2014) 363–380.

[23] H. Gao, H. Li, L-P. Wang, Lattice Boltzmann simulation of turbulent flow laden with finite-size particles, Comp.& Math. Appl., 65 (2013) 194–210.

[24] C. Peng., Y. H. Teng, B. Huang, Z.-L. Guo, L.-P. Wang, Implementation issues and benchmarking of lattice Boltzmann method for moving particle simulations in a viscous flow, Comp.& Math. Applications, (2015), DOI: 10.1016/j.camwa.2015.08.027.

[25] Suga K., Kuwata Y., Takashima K., Chikasue R., A D3Q27 multiple-relaxation-time lattice Boltzmann method for turbulent flows, Comp.& Math. Applications, 69(2015): 518–529.

[26] P. Lammers, K.N. Beronov, R. Volkert, G. Brenner, F. Durst, Lattice BGK direct numerical simulation of fully developed turbulence in incompressible plane channel flow, Computers & Fluids, 35 (2006) 1137–1153.

[27] He X., Luo L.-S., Dembo M., Some progress in lattice Boltzmann method. Part I. Nonuniform mesh grids, J. Comp. Phys., 129 (1996) 357–363.

[28] Niu X.D., Chew Y.T., Shu C., Simulation of flows around an impulsively started circular cylinder by Taylor series expansion and least squares-based lattice Boltzmann method, J. Comp. Phys., 188 (2003) 176–193.

[29] Filippova O., Hänel, Boundary-fitting and local grid refinement for lattice-BGK models, Int. J. Modern Phys. C, 9 (1998) 1271–1279.

[30] Cao N., Chen S., Jin S., et al, Physical symmetry and lattice symmetry in the lattice Boltzmann method, Phys. Rev. E, 55 (1997) R21-R24.

[31] A. Bardow , I. Karlin V., A. A. Gusev , General characteristic-based algorithm for off-lattice Boltzmann simulatiions, Europhys. Lett., 73 (2006) 434–440.

[32] M. Bouzidi , D. dHumi'eres , P. Lallemand , et al, Lattice Boltzmann Equation on a two-dimensional rectangular grid, J. Comp. Phys. 172 (2001) 704–717.

[33] Zong Y., Peng C., Z. Guo, et al, Designing Correct Fluid Hydrodynamics on A Rectangular Grid using MRT Lattice Boltzmann Approach, Comp.& Math. Applications, (2015), DOI: 10.1016/j.camwa.2015.05.021.

[34] Zhou J., Rectangular lattice Boltzmann method, Phys. Rev. E, 81(2010) 026705.

[35] Zhou J., MRT rectangular lattice Boltzmann method, Inter. J. Modern Phys. C, 23 (2012) 1250040.

[36] Chikatamarla S., Karlin I., Comment on Rectangular lattice Boltzmann method, Phys. Rev. E., 83 (2011) 048701.

[37] Hegele L. Jr., Mattila K., Philippi P., Rectangular lattice Boltzmann schemes with BGK-collision operator, J Sci. Comput., 56 (2013) 230–242.

[38] Jiang B., Zhang X., Philippi P., An orthorhombic lattice Boltzmann model for pore-scale simulation of fluid flow in porous media, Transp. Porous Med. (2014) 104:145–159.

[39] C. Peng, H. D. Min, Z. Guo, L.-P. Wang, 2016, A hydrodynamically-consistent MRT lattice Boltzmann model on a 2D rectangular grid, submitted to J. Comp. Phys.

[40] Inamuro T., A lattice kinetic scheme for incompressible viscous flows with heat transfer, Phil. Trans. R. Soc. Lond. A, 360 (2002) 477–484.

[41] Yoshino M., Hotta Y., Hirozane T.,*et al.* , A numerical method for incompressible non-Newtonian fluid flows based on the lattice Boltzmann method, J Non-Newton. Fluid Mech., 147 (2007) 69–78.

[42] Wang L., Mi J., Meng X., *et al.* , A localized mass-conserving lattice Boltzmann approach for non-Newtonian fluid flows, Commun. Comput. Phys., 17 (2015) 908–924.

[43] C. Peng, Z.-L. Guo, L.-P. Wang, 2016, A lattice-BGK model for the Navier-Stokes equations based on a rectangular grid, submitted to Comp.& Math. Appl.

[44] Z.-H. Chai and T.-S. Zhao, Effect of the forcing term in the multiple-relaxation-time lattice Boltzmann equation on the shear stress or the strain rate tensor, Phys. Rev. E 86, 016705 (2012).

[45] X. He, Q. Zou, and L.-S. Luo, Analytic solutions of simple flows and analysis of nonslip boundary conditions for the lattice Boltzmann BGK model, J. Stat. Phys. 87, 115 (1997).

[46] L.-S. Luo, Unified Theory of Lattice Boltzmann Models for Nonideal Gases, Phys. Rev. Lett. 81 (8) (1998) 1618–1621.

[47] L.-S. Luo, Theory of the lattice Boltzmann method: Lattice Boltzmann models for nonideal gases, Phys. Rev. E 62 (4) (2000) 4982–4996.

[48] N. S. Martys, X. Shan, and H. Chen, Evaluation of the external force term in the discrete Boltzmann equation, Phys. Rev. E 58, 6855 (1998).

[49] A. J. C. Ladd and R. Verberg, Lattice-Boltzmann Simulations of Particle-Fluid Suspensions, J. Stat. Phys. 104, 1191 (2001).

[50] J.M. Buick and C.A. Greated, Gravity in a lattice Boltzmann model, Phys. Rev. E 61, 5307 (2000).

[51] Z. Guo, C. Zheng, B. Shi, Discrete lattice effects on the forcing term in the lattice Boltzmann method, Phys. Rev. E 65 (046308) (2002) 1–6.

[52] A. A. Mohamad, A. Kuzmin, A critical evaluation of force term in lattice Boltzmann method, natural convection problem, International J. of Heat & Mass Transfer, 53 (2010) 990–996.

[53] S. Farnoush, M. T. Manzari, An investigation on the body force modeling in a lattice Boltzmann BGK simulation of generalized Newtonian fluids, Physica A 415, (2014) 315–332.

[54] K. N. Premnath, M. J. Pattison, S. Banerjee, Generalized lattice Boltzmann equation with forcing term for computation of wall-bounded turbulent flows, Phys. Rev. E 79, 026703 (2009).

[55] H. D. Min, C. Peng, Z.-L. Guo, L.-P. Wang, 2016, An inverse design analysis of mesoscopic implementation of non-uniform forcing in MRT lattice Boltzmann models, submitted to Comp.& Math. Appl.

[56] Taylor, G.I. and Green, A.E., 1937, Mechanism of the production of small eddies from large ones. Proc. Royal Soc. London, A, 158: 499-521.

[57] Bo Y, Wang P, Guo ZL, Wang L-P, Parallel implementation and validation of DUGKS for three-dimensional Taylor-Green vortex flow and turbulent channel flow, submitted to Computers and Fluids.

[58] V. Eswaran and S. B. Pope, 1988, An examination of forcing in direct numerical simulations of turbulence, Comput. Fluids 16, 257-278.

[59] Amati G., Succi S., Piva R., Massively parallel lattice-Boltzmann simulation of turbulent channel flow, Int J Mod Phys C, 8 (1997): 869–878.

[60] Toschi F., Amati G., Succi S., Benzi R., Piva R., Intermittency and structure functions in channel flow turbulence, Phys Rev Lett, 82 (1999): 5044–7.

[61] Kim, J., Moin, P., and Moser, R., Turbulence Statistics in Fully-Developed Channel Flow at Low Reynolds-Number, J. FluidMech., 177 (1987) 133-166.

[62] Moser, R., Kim, J., and Mansour, N. N., Direct Numerical Simulation of Turbulent Channel Flow up to Re-Tau = 590, Phys. Fluids., 11 (1999) 943-945.

[63] Wang L-P, Peng C., Guo Z-L, Yu Z-S, Flow Modulation by Finite-Size Neutrally Buoyant Particles in a Turbulent Channel Flow, ASME J. of Fluids Engr., 138 (2016) 041103.

[64] S. Hoyas, J. Jimenez, Reynolds number effects on the Reynolds-stress budgets in turbulent channels, Phys. Fluids, 20 (2008) 101511.

[65] J. Jimenez, S. Hoyas, Turbulent fluctuations above the buffer layer of wall-bounded flows, J. Fluid Mech. 611 (2008) 215-236.

[66] Wang L-P, Peng C., Guo Z-L, Yu Z-S, Lattice Boltzmann Simulation of Particle-Laden Turbulent Channel Flow, Computers and Fluids, 124 (2016) 226-236.

[67] J. D. Sterling and S. Chen, 1996, Stability analysis of lattice Boltzmann methods, J. Comput. Phys. 123, 196–206 (1995).

[68] R.A. Worthing, J. Mozer, G. Seeley, Stability of lattice Boltzmann methods in hydrodynamic regimes, Phys. Rev. E 56 (1997) 2243–2253.

[69] X.D. Niu, C. Shu, Y.T. Chew, T.G. Wang, Investigation of stability and hydrodynamics of different lattice Boltzmann models, J. Stat. Phys. 117 (3–4) (2004) 665–680.

[70] D. Ricot, S. Mari, P. Sagaut, C. Bailly, Lattice Boltzmann method with selective viscosity filter, Journal of Computational Physics 228 (2009) 4478–4490.

[71] Y. G. Cheng and H. Zhang, A viscosity counteracting approach in the lattice Boltzmann BGK model for low viscosity flow: Preliminary verification, Comput. Math. Appl., 61 (2011), pp. 3690–3702.

[72] C. Zhang, Y. Cheng, S. Huang and J. Wu (2016). Improving the Stability of the Multiple-Relaxation-Time Lattice Boltzmann Method by a Viscosity Counteracting Approach. Advances in Applied Mathematics and Mechanics, 8, pp 37-51 doi:10.4208/aamm.2014.m512

Appendix A

CALCULATION OF VELOCITY GRADIENTS

As mentioned in Sec. 2, the added part of equilibrium moments, $m_i^{(eq,1)}$, is composed of a set of 9 coefficients h_{ij}, λ, and the strain-rate tensor $(\partial_\beta u_\alpha + \partial_\alpha u_\beta)/2$. Therefore, we need to update the strain-rate components at each time step and apply them in the collision term. By design, all the strain-rate components can be calculated based on the non-equilibrium moments. The derivation is a bit tedious, we only present the final results here.

First, from Eq. (2.23) we observe that $\mathbf{m}^{(1)}$ is related to equilibrium moments and forcing. To separate the two, we define an array G_i as the part of $\mathbf{m}^{(1)}$ without any forcing involved. According to our derivation, we shall have $G_i = \mathbf{M}_{ij} f_j - m_i^{(eq,0)} + \delta_t \Psi_i / (2 - s_i)$, where $\mathbf{M}, m_i^{(eq,0)}, \Psi_i$ and s_i are defined in Sec. 2. Then, the strain-rate components can be calculated according to

$$
\begin{cases}
\partial_x u = \left(C_1 B_4 - C_2 B_2\right) / \left(B_1 B_4 - B_2 B_3\right), \\
\partial_y v = \left(C_2 B_1 - C_1 B_3\right) / \left(B_1 B_4 - B_2 B_3\right), \\
\partial_z w = \left[G_2 / \left(\rho_0 \delta_t c^2\right) - r_{11}\partial_x u - r_{12}\partial_y v\right] / r_{13}, \\
\partial_y u + \partial_x v = G_{14}/c_1, \\
\partial_z v + \partial_y w = G_{15}/c_2, \\
\partial_z u + \partial_x w = G_{16}/c_3,
\end{cases}
\qquad
\begin{cases}
B_1 = r_{11} r_{23} - r_{13} r_{21}, \\
B_2 = r_{12} r_{23} - r_{13} r_{22}, \\
B_3 = r_{23} r_{31} - r_{21} r_{33}, \\
B_4 = r_{23} r_{32} - r_{22} r_{33}, \\
C_1 = \left(r_{23} G_2 - r_{13} G_{10}\right) / \left(\rho_0 \delta_t c^2\right), \\
C_2 = \left(r_{23} G_{12} - r_{33} G_{10}\right) / \left(\rho_0 \delta_t c^2\right),
\end{cases}
\tag{A.1}
$$

where $c_1 = \rho_0 \delta_t c^2 \lambda / a - a \rho_0 \delta_t c^2 \kappa_3 / (10 s_c)$, $c_2 = \rho_0 \delta_t c^2 \left[0.1 s_c^* \kappa_3 \left(a^2 b^2 - a^2\right) + \lambda\right] / (ab) - ab \rho_0 \delta_t c^2 \kappa_3 / (10 s_c)$,

$c_3 = \rho_0 \delta_t c^2 \left[0.1 s_c^* \kappa_3 \left(b^2 - a^2\right) + \lambda\right] / b - b \rho_0 \delta_t c^2 \kappa_3 / \left(10 s_c\right)$, $s_c^* = \left(2 - s_c\right) / \left(2 s_c\right)$, and $\kappa_3 = \gamma + 4$. Other parameters have been defined in Sec. 2. The coefficients r_{ij} are given as

$$r_{ij} = h_{ij} + \begin{bmatrix} \left(\kappa_1 \frac{c_s^2}{c^2} - \frac{9+\gamma}{5}\right) \frac{19}{s_e} & \left(\kappa_1 \frac{c_s^2}{c^2} - \frac{9+a\gamma_a}{5}\right) \frac{19}{s_e} & \left(\kappa_1 \frac{c_s^2}{c^2} - \frac{9+b\gamma_b}{5}\right) \frac{19}{s_e} \\ \left(\kappa_3 \frac{c_s^2}{c^2} - \frac{6-\gamma}{5}\right) \frac{1}{s_n} & \left(\kappa_3 \frac{c_s^2}{c^2} + \frac{6-a\gamma_a}{5}\right) \frac{1}{s_n} & \left(\kappa_3 \frac{c_s^2}{c^2} + \frac{6-b\gamma_b}{5}\right) \frac{1}{s_n} \\ \kappa_2 \frac{c_s^2}{c^2} \frac{1}{s_n} & \left(\kappa_2 \frac{c_s^2}{c^2} - \frac{6-a\gamma_a}{10}\right) \frac{1}{s_n} & \left(\kappa_2 \frac{c_s^2}{c^2} + \frac{6-b\gamma_b}{10}\right) \frac{1}{s_n} \end{bmatrix} \tag{A.2}$$

where $\kappa_1 = 1/a^2 + 1/b^2 + 1$, $\kappa_2 = 1/a^2 - 1/b^2$, $\kappa_3 = 2 - 1/a^2 - 1/b^2$, $\gamma_a = a\left(\gamma + 4\right) - 4/a$, $\gamma_b = b\left(\gamma + 4\right) - 4/b$ and h_{ij} are defined in Eq. (2.28).